

Streaming Operator Inference for Model Reduction of Large-Scale Dynamical Systems[★]

Tomoki Koike^{a,*}, Prakash Mohan^c, Mark T. Henry de Frahan^c, Julie Bessac^c, Elizabeth Qian^{a,b}

^a School of Aerospace Engineering, Georgia Institute of Technology, Atlanta, 30332, GA, USA

^b School of Computational Science and Engineering, Georgia Institute of Technology, Atlanta, 30332, GA, USA

^c Computational Science Center, National Laboratory of the Rockies (NLR), 15013 Denver West Parkway, Golden, 80401, CO, USA

Abstract

Projection-based model reduction enables efficient simulation of complex dynamical systems by constructing low-dimensional surrogate models from high-dimensional data. The Operator Inference (OpInf) approach learns such reduced surrogate models through a two-step process: constructing a low-dimensional basis via Singular Value Decomposition (SVD) to compress the data, then solving a linear least-squares (LS) problem to infer reduced operators that govern the dynamics in this compressed space, all without access to the underlying code or full model operators, i.e., non-intrusively. Traditional OpInf operates as a batch learning method, where both the SVD and LS steps process all data simultaneously. This poses a barrier to deployment of the approach on large-scale applications where data set sizes prevent the loading of all data into memory simultaneously. Additionally, the traditional batch approach does not naturally allow model updates using new data acquired during online computation. To address these limitations, we propose Streaming OpInf, which learns reduced models from sequentially arriving data streams. Our approach employs incremental SVD for adaptive basis construction and recursive LS for streaming operator updates, eliminating the need to store complete data sets while enabling online model adaptation. The approach can flexibly combine different choices of streaming algorithms for numerical linear algebra: we systematically explore the impact of these choices both analytically and numerically to identify effective combinations for accurate reduced model learning. Numerical experiments on benchmark problems and a large-scale turbulent channel flow demonstrate that Streaming OpInf achieves accuracy comparable to batch OpInf while reducing memory requirements by over 99% and enabling dimension reductions exceeding 31,000x, resulting in orders-of-magnitude faster predictions. Our results establish Streaming OpInf as a scalable framework for reduced operator learning in large-scale and online streaming settings.

Keywords: model reduction, operator inference, data streaming, incremental SVD, recursive least-squares

1. Introduction

The ability to use data to learn accurate and efficient reduced models for complex dynamical systems is crucial across scientific and engineering applications, as these models facilitate rapid simulations for many-query computations such as uncertainty quantification, inverse problems, optimization, and control.

Operator Inference (OpInf) [1, 2] refers to a family of methods that learn such efficient reduced models from data by fitting reduced model operators to minimize the residual of the reduced system equations. OpInf assumes a polynomial reduced model, where the learned operators are coefficient matrices representing polynomial nonlinearities. The formulation hinges on two key steps: (i) dimension reduction by projecting data onto a reduced basis constructed via Proper Orthogonal Decomposition (POD), which computes an optimal low-dimensional approximation via Singular Value Decomposition (SVD), and (ii) solving a linear least-squares (LS) problem to compute the reduced operators

[★]The authors were supported by the Department of Energy Office of Science Advanced Scientific Computing Research, DOE Award DE-SC0024721.

*Corresponding author

Email address: tkoike@gatech.edu (Tomoki Koike)

by fitting them to all projected data at once. The first step emanates from classical projection-based model reduction, which projects the full-dimensional model onto a low-dimensional subspace to yield accurate yet computationally efficient reduced models [3], while the second step leverages data-driven learning to infer reduced operators without intrusive access to the underlying code or full model operators, and thereby making OpInf a *non-intrusive* method.

The two-step *reduce-then-learn* formulation of OpInf is highly amenable to extensions. Some researchers modify the projection step by replacing the linear POD basis with nonlinear manifolds [4–6] or adopting oblique projections [7]. Others alter the learning step through regularized or constrained formulations for robustness [8–10], tensor or nested operator training for scalability [11, 12], Bayesian or Gaussian process regression for uncertainty quantification [13, 14], or physics-informed constraints on coefficients for stability and structure preservation [15–21]. The work [22] reverses the standard workflow by first learning full-dimensional operators and then projecting them onto a reduced basis. Complementary strategies include data reprojection for noise attenuation [23, 24], variable lifting to extend OpInf to non-polynomial systems [25], and exact reconstruction of intrusive operators [26]. These extensions have enabled vast applications across fluid dynamics [8, 27], mechanical systems [28–31], chemical kinetics [32], ice sheet modeling [12, 26], plasma turbulence [33], aeroelastic flutter [34], and solar wind dynamics [35].

However, OpInf and other existing reduced model learning methods [36–38] are typically *batch* learning methods which rely on collecting ample data over time, storing them in their entirety, and then learning the reduced models offline by processing all data at once. However, many real-world applications—such as climate modeling [39–41], fluid dynamics [42–44], and astrophysics [45–47]—present two critical challenges. First, high-resolution simulations generate *large-scale* datasets requiring terabytes to petabytes of storage [48, 49], making it infeasible to store all data in memory or on disk. Second, some large-scale applications such as digital twins [50, 51], system monitoring [52], and anomaly detection [53] often demand online model learning for *real-time* decision-making and control, which limits the possibility of waiting for complete data collection before training [49]. Hence, in this work, we propose a new reduced model learning paradigm based on *streaming* data, where state snapshots and possibly their time derivatives arrive sequentially with only a small subset accessible at any given moment, thereby achieving significant memory savings while enabling real-time model updates and predictions.

To address memory and storage challenges, parallel/distributed computing [54] and domain decomposition methods [55–58] for OpInf have been proposed. The parallel approach distributes data and basis computation across multiple processors, aggregates results to obtain reduced data, and then computes the reduced operators. Domain decomposition methods exploit spatial locality by dividing the domain into subdomains, learning reduced models within each, and coupling them to form a global model. Similar strategies have been applied to other model reduction techniques [59–65].

While these approaches can make learning reduced models tractable for some large-scale problems by partitioning the data set along rows, they remain batch methods in the sense that each partition requires simultaneous access to all time snapshots. In contrast, exploitation of temporal partitioning, where data can be processed incrementally column-by-column as snapshots arrive, remains largely unexplored. This motivates our development of *Streaming OpInf*, which reformulates the two main components of OpInf for streaming data by using streaming SVD formulations for data reduction and using a Recursive Least Squares (RLS) formulation to solve the reduced operator learning problem. In summary, this work makes the following contributions:

1. We propose a streaming approach to OpInf that learns reduced models incrementally as data arrives, enabling scalability to large-scale datasets and laying the groundwork for real-time model updates and predictions.
2. We implement and compare several state-of-the-art streaming algorithms from numerical linear algebra for reduced basis construction and operator learning, including incremental Singular Value Decomposition (iSVD) methods [66], randomized streaming SVD [67], and RLS variants [68, 69], evaluating their accuracy, memory requirements, and computational efficiency.
3. We demonstrate that Streaming OpInf achieves significant memory savings compared to batch OpInf while learning accurate reduced models from streaming data on benchmark problems and a large-scale turbulent three-dimensional channel flow simulation with nearly 10 million degrees of freedom.

Batch processing challenges have motivated streaming approaches for other operator learning and modal analysis methods such as Dynamic Mode Decomposition (DMD), spectral POD, and their variants, which identify a system's natural frequencies, damping factors, and mode shapes [70, 71]. Streaming versions of spectral POD [72] and

quadratic manifold construction [73] employ iSVD for incremental basis construction but focus solely on extracting reduced manifolds without addressing operator learning. Streaming DMD [74–76] uses RLS or rank-1 updates to incrementally update decompositions, with extensions including parallel [77] and adaptive [78, 79] settings. While DMD enables both analysis and prediction, it differs fundamentally from OpInf in its treatment of nonlinear systems. That is, DMD identifies linear dynamics either directly or through the Koopman framework [80, 81], where nonlinear dynamics are embedded into a higher-dimensional space with linear evolution. This lifting introduces practical challenges including approximation errors from finite-dimensional truncation of the infinite-dimensional Koopman operator and potentially large lifted dimensions that negate computational benefits. This challenge of learning reduced operators in the lifted space arises in another similar work of online robust Koopman operator learning [82]. In contrast, OpInf directly learns polynomial operators in the reduced space without such lifting.

Another related work, Streaming weak-SINDy [83], learns weak-form partial differential equation (PDE) solutions in a streaming fashion. The method accumulates feature and target matrices via streaming integration with streaming POD, deferring regression to an offline stage where sequential thresholding LS requires solving the batch LS problem repeatedly until sparsity is achieved, whereas we consider online updating of the LS solution via RLS along with different combinations of algorithms for streaming reduced operator learning. All existing streaming methods introduced so far show growing recognition that incremental learning is essential for scalability and real-time adaptation. However, we emphasize that no existing approach combines dimension reduction via incremental basis updates with direct learning of reduced polynomial operators from streaming data, which is the contribution of our Streaming OpInf framework.

The remainder of this paper is organized as follows. Section 2 reviews OpInf and the key ingredients of Streaming OpInf: streaming SVD and RLS. Section 3 presents the Streaming OpInf formulation with guidance on algorithm selection for incremental basis construction and operator learning. Section 4 demonstrates effectiveness on benchmark problems and a large-scale turbulent three-dimensional channel flow simulation. Section 5 summarizes findings and discusses future directions.

2. Background

In Section 2.1, we provide the necessary background on OpInf for reduced operator learning. We then introduce the streaming numerical linear algebra methods upon which our proposed streaming operator learning framework is built, beginning with streaming SVD methods in Section 2.2 and finishing with recursive least squares methods in Section 2.3.

2.1. The Operator Inference Problem

In this work, we consider an n -dimensional ordinary differential equation (ODE) with a quadratic nonlinearity in the state vector $\mathbf{x}(t) \in \mathbb{R}^n$:

$$\dot{\mathbf{x}}(t) = \mathbf{A}_1 \mathbf{x}(t) + \mathbf{A}_2(\mathbf{x}(t) \otimes \mathbf{x}(t)) + \mathbf{B}\mathbf{u}(t) + \mathbf{c}, \quad (1)$$

where \otimes denotes the Kronecker product. The system evolves over time $t \in [0, T]$ from an initial condition $\mathbf{x}(0) = \mathbf{x}_0$. Here, \mathbf{A}_1 and \mathbf{A}_2 are the linear and quadratic operators, $\mathbf{B} \in \mathbb{R}^{n \times m}$ is the input-to-state mapping for a bounded input $\mathbf{u} \in \mathbb{R}^m$ with $m \ll n$, and $\mathbf{c} \in \mathbb{R}^n$ is a constant term representing a mean shift or other affine contribution. This linear-quadratic structure in (1) is representative but not restrictive; the OpInf framework accommodates alternative polynomial structures, including cubic or higher-order terms, as well as systems without input or constant terms. We demonstrate this flexibility in Section 4.

This work is motivated by the setting where n is on the order of millions or larger, as commonly arises from spatial discretization of PDEs. We assume that the matrix operators in (1) are unavailable in explicit form (i.e., non-intrusive). Our goal is to learn a reduced model of dimension $r \ll n$ from sampled data that enables rapid, accurate prediction. Specifically, we assume that the following data are available: K state snapshots $\{\mathbf{x}_k\}_{k=1}^K$ and their corresponding time derivatives $\{\dot{\mathbf{x}}_k\}_{k=1}^K$ and input snapshots $\{\mathbf{u}_k\}_{k=1}^K$. These data usually correspond to saving the numerical solution of (1) at discrete times t_1, \dots, t_K . If time derivatives are not directly available they may be approximated via finite differences.

To learn a reduced model, we employ OpInf [1], which follows a *reduce-then-learn* paradigm: first project the high-dimensional data onto a low-dimensional subspace, then solve a data-driven regression problem to learn reduced operators from the projected data to obtain a reduced model that preserves the polynomial structure of (1). This approach avoids access to the underlying code or full operators in (1). We summarize these two key steps below:

1. Reduction step: This step constructs a reduced basis via POD [84–86] and projects the data onto this basis. Let us form the snapshot matrix $\mathbf{X} = [\mathbf{x}_1, \dots, \mathbf{x}_K] \in \mathbb{R}^{n \times K}$ from the sampled snapshots. POD is based on the SVD $\mathbf{X} = \mathbf{V}\Sigma\mathbf{W}^\top$, where $\mathbf{V} \in \mathbb{R}^{n \times \ell}$ and $\mathbf{W} \in \mathbb{R}^{K \times \ell}$ are orthogonal matrices satisfying $\mathbf{V}^\top \mathbf{V} = \mathbf{W}^\top \mathbf{W} = \mathbf{I}_\ell$, and $\Sigma \in \mathbb{R}^{\ell \times \ell}$ is a diagonal matrix with singular values $\sigma_1 \geq \dots \geq \sigma_\ell \geq 0$ for $\ell \leq \min\{n, K\}$. The POD basis $\mathbf{V}_r \in \mathbb{R}^{n \times r}$ is then constructed from the leading r left singular vectors that capture the dominant energy modes. Further, define the reduced state $\hat{\mathbf{x}}(t) = \mathbf{V}_r^\top \mathbf{x}(t) \in \mathbb{R}^r$. Projecting the K snapshots onto the POD basis yields reduced states $\{\hat{\mathbf{x}}_k\}_{k=1}^K = \{\mathbf{V}_r^\top \mathbf{x}_k\}_{k=1}^K$ and reduced time derivatives $\{\dot{\hat{\mathbf{x}}}_k\}_{k=1}^K = \{\mathbf{V}_r^\top \dot{\mathbf{x}}_k\}_{k=1}^K$. This reduced data is the basis of the operator learning step.

2. Learning step: Using the projected data, infer the reduced operators:

$$\dot{\hat{\mathbf{x}}}(t) = \hat{\mathbf{A}}_1 \hat{\mathbf{x}}(t) + \hat{\mathbf{A}}_2 (\hat{\mathbf{x}}(t) \otimes \hat{\mathbf{x}}(t)) + \hat{\mathbf{B}} \mathbf{u}(t) + \hat{\mathbf{c}}, \quad (2)$$

where $\hat{\mathbf{A}}_1 \in \mathbb{R}^{r \times r}$, $\hat{\mathbf{A}}_2 \in \mathbb{R}^{r \times r^2}$, $\hat{\mathbf{B}} \in \mathbb{R}^{r \times m}$, and $\hat{\mathbf{c}} \in \mathbb{R}^r$ are determined by solving the regularized LS problem:

$$\min_{\hat{\mathbf{A}}_1, \hat{\mathbf{A}}_2, \hat{\mathbf{B}}, \hat{\mathbf{c}}} \frac{1}{K} \sum_{k=1}^K \|\dot{\hat{\mathbf{x}}}_k - \hat{\mathbf{A}}_1 \hat{\mathbf{x}}_k - \hat{\mathbf{A}}_2 (\hat{\mathbf{x}}_k \otimes \hat{\mathbf{x}}_k) - \hat{\mathbf{B}} \mathbf{u}_k - \hat{\mathbf{c}}\|_2^2 + \|\Gamma^{1/2} [\hat{\mathbf{A}}_1, \hat{\mathbf{A}}_2, \hat{\mathbf{B}}, \hat{\mathbf{c}}]^\top\|_F^2, \quad (3)$$

where the symmetric positive definite matrix $\Gamma \in \mathbb{R}^{d \times d}$ with $d = r + r^2 + m + 1$ defines a Tikhonov regularization term [8].

When the fitted model (2) has the same polynomial structure as (1), unregularized OpInf with $\Gamma = \mathbf{0}_{d \times d}$ recovers the intrusive Galerkin projection operators under certain conditions [1, Thm. 1]. However, regularization is particularly important in the streaming setting due to error accumulation over many operator updates, as we will discuss in Section 3.

The OpInf problem (3) may be expressed as a standard regularized linear LS problem as follows:

$$(\text{OpInf}) \quad \min_{\mathbf{O}} \frac{1}{K} \|\mathbf{R} - \mathbf{DO}\|_F^2 + \|\Gamma^{1/2} \mathbf{O}\|_F^2, \quad (4)$$

where the right-hand side, data, and operator matrices are defined to be

$$\mathbf{R} = [\dot{\hat{\mathbf{x}}}_1, \dots, \dot{\hat{\mathbf{x}}}_K]^\top \in \mathbb{R}^{K \times r}, \quad \mathbf{D} = [\hat{\mathbf{X}}^\top, (\hat{\mathbf{X}} \odot \hat{\mathbf{X}})^\top, \mathbf{U}^\top, \mathbf{1}_K] \in \mathbb{R}^{K \times d}, \quad \mathbf{O} = [\hat{\mathbf{A}}_1, \hat{\mathbf{A}}_2, \hat{\mathbf{B}}, \hat{\mathbf{c}}]^\top \in \mathbb{R}^{d \times r}, \quad (5)$$

with

$$\hat{\mathbf{X}} = [\hat{\mathbf{x}}_1, \dots, \hat{\mathbf{x}}_K] \in \mathbb{R}^{r \times K}, \quad \hat{\mathbf{X}} \odot \hat{\mathbf{X}} = [\hat{\mathbf{x}}_1 \otimes \hat{\mathbf{x}}_1, \dots, \hat{\mathbf{x}}_K \otimes \hat{\mathbf{x}}_K] \in \mathbb{R}^{r^2 \times K}, \quad \mathbf{U} = [\mathbf{u}_1, \dots, \mathbf{u}_K] \in \mathbb{R}^{m \times K}, \quad (6)$$

where $\mathbf{1}_K \in \mathbb{R}^K$ is a vector of ones and \odot denotes the Khatri-Rao product (column-wise Kronecker product).

Alternatively, augmenting the data and right-hand side matrices yields the following linear least squares formulation:

$$\min_{\mathbf{O}} \frac{1}{K} \|\bar{\mathbf{R}} - \bar{\mathbf{D}} \mathbf{O}\|_F^2, \quad \text{where} \quad \bar{\mathbf{D}} = \begin{bmatrix} \mathbf{D} \\ \Gamma^{1/2} \end{bmatrix} \in \mathbb{R}^{(K+d) \times d} \quad \text{and} \quad \bar{\mathbf{R}} = \begin{bmatrix} \mathbf{R} \\ \mathbf{0}_{d \times r} \end{bmatrix} \in \mathbb{R}^{(K+d) \times r}. \quad (7)$$

If \mathbf{D} has full column rank, this overdetermined system has unique solution $\mathbf{O} = \bar{\mathbf{D}}^\dagger \bar{\mathbf{R}}$.

Standard OpInf is a *batch* method built on standard direct computation of the SVD and direct solution of the LS problem. These approaches load and store the entire data set in working memory, which is infeasible for real-time streaming data settings and large-scale problems. While distributed computing [54] and domain decomposition [56] address the memory bottleneck, we pursue an alternative by adapting OpInf to the streaming setting, where snapshots $\mathbf{x}_1, \dots, \mathbf{x}_K$ are processed incrementally as they arrive. This requires two key ingredients: (i) incremental basis construction via iSVD, and (ii) recursive operator learning via RLS which we now introduce.

2.2. Streaming SVD Methods

We seek to address the high memory cost of $O(n(K + r))$ in standard SVD for storing the data and basis, by introducing two streaming SVD algorithms, Baker's iSVD [66] and SketchySVD [67].

2.2.1. Baker's iSVD Algorithm

Assume at time step k we have streamed snapshots $[\mathbf{x}_1, \dots, \mathbf{x}_k]$ and computed a rank- r_k SVD of the data matrix $\mathbf{X}_k \in \mathbb{R}^{n \times k}$ as $\mathbf{X}_k = \mathbf{V}_{r_k} \boldsymbol{\Sigma}_{r_k} \mathbf{W}_{r_k}^\top$, where $k \in \{1, \dots, K\}$ and $r_k \leq r$.

The core innovation in iSVD algorithms [66, 87–91] is efficiently updating the SVD components when a new snapshot \mathbf{x}_{k+1} arrives. This rank-1 increment is based on the identity:

$$[\mathbf{V}_{r_k} \boldsymbol{\Sigma}_{r_k} \mathbf{W}_{r_k}^\top \quad \mathbf{x}_{k+1}] = [\mathbf{V}_{r_k} \quad \mathbf{x}_\perp / p] \begin{bmatrix} \boldsymbol{\Sigma}_{r_k} & \mathbf{q} \\ \mathbf{0}_{1 \times r_k} & p \end{bmatrix} \begin{bmatrix} \mathbf{W}_{r_k} & \mathbf{0}_{k \times 1} \\ \mathbf{0}_{1 \times r_k} & 1 \end{bmatrix}^\top = \hat{\mathbf{V}} \mathbf{J} \hat{\mathbf{W}}^\top, \quad (8)$$

where $\mathbf{q} = \mathbf{V}_{r_k}^\top \mathbf{x}_{k+1} \in \mathbb{R}^{r_k}$, $\mathbf{x}_\perp = \mathbf{x}_{k+1} - \mathbf{V}_{r_k} \mathbf{q} \in \mathbb{R}^n$, and $p = \|\mathbf{x}_\perp\|_2$. Here, \mathbf{V}_{r_k} is augmented by the normalized residual \mathbf{x}_\perp / p , creating a small $(r_k + 1) \times (r_k + 1)$ intermediate matrix \mathbf{J} , while the rightmost matrix expands \mathbf{W}_{r_k} to accommodate the new snapshot.

The SVD matrices are then updated by computing $\mathbf{V}_J \boldsymbol{\Sigma}_J \mathbf{W}_J^\top = \text{svd}(\mathbf{J})$ and setting

$$\mathbf{V}_{r_{k+1}} = \hat{\mathbf{V}} \mathbf{V}_J, \quad \boldsymbol{\Sigma}_{r_{k+1}} = \boldsymbol{\Sigma}_J, \quad \mathbf{W}_{r_{k+1}} = \hat{\mathbf{W}} \mathbf{W}_J. \quad (9)$$

In this work, we employ Baker's iSVD framework [66], which builds on these identities (8) and (9) while addressing two key challenges in standard iSVD methods: determining whether new snapshots warrant basis updates (typically via residual norm p thresholding [91]) and maintaining numerical stability against accumulated errors (often requiring ad-hoc reorthogonalization [91, 92]). Baker's algorithm eliminates update determination by enforcing strict orthonormality at every iteration via double orthogonalization: after projecting the new data vector, it applies Gram-Schmidt orthogonalization followed by QR decomposition on the residual, $\mathbf{x}_\perp / p \leftarrow \text{qr}(\mathbf{x}_\perp)$. This approach, similar to [93], ensures numerical accuracy without additional reorthogonalization steps. For completeness, we summarize Baker's iSVD algorithm in Algorithm 1.

2.2.2. Randomized SketchySVD Algorithm

Rather than updating the SVD components at each iteration as in Baker's iSVD, SketchySVD [67] is a randomized algorithm that computes the truncated SVD by multiplying the data with predefined random matrices to compress them into low-dimensional randomized *sketches* during streaming and computing the final SVD only after processing the entire dataset.

Let the sketch sizes be denoted q and s , which control the dimensions of the compressed representations and determine the accuracy-memory tradeoff. SketchySVD maintains three randomized sketches $\mathcal{X}_{\text{range}} \in \mathbb{R}^{n \times q}$, $\mathcal{X}_{\text{corange}} \in \mathbb{R}^{q \times K}$, $\mathcal{X}_{\text{core}} \in \mathbb{R}^{s \times s}$ that capture the range, corange, and core information (information to improve the estimate of the singular values and vectors) of the data matrix \mathbf{X} , respectively [67]. These sketches are formed as products of \mathbf{X} with four fixed random reduction maps $\Upsilon \in \mathbb{R}^{q \times n}$, $\Omega \in \mathbb{R}^{q \times K}$, $\Xi \in \mathbb{R}^{s \times n}$, $\Psi \in \mathbb{R}^{s \times K}$:

$$\mathcal{X}_{\text{range}} = \mathbf{X} \Omega^\top, \quad \mathcal{X}_{\text{corange}} = \Upsilon \mathbf{X}, \quad \mathcal{X}_{\text{core}} = \Xi \mathbf{X} \Psi^\top.$$

These randomized sketches preserve essential geometric and algebraic properties (norms, inner products, and low-rank structure) of the original data, enabling memory-efficient approximate SVD recovery with high probability [94]. In this work, we employ *sparse sign matrices* for the four random reduction maps to reduce the computational cost of matrix-vector and matrix-matrix multiplications when updating sketches with each new data stream (see [95] for additional details). Note that other types of random matrices, such as Gaussian and subsampled randomized Fourier transform (SRFT) matrices, can also be used [67].

After processing all snapshots, the algorithm computes QR decompositions of the range and corange sketches, forms a small core matrix $\mathbf{C} \in \mathbb{R}^{s \times s}$, computes its SVD, and combines these results to construct the approximate SVD of \mathbf{X} . To ensure a truncated SVD with sufficiently tight theoretical error bounds, the recommended sketch sizes are $q = 4r + 1$ and $s = 2q + 1$ [67]. The SketchySVD algorithm is summarized in Algorithm 2, with comprehensive details available in [67].

2.2.3. Cost and Error Analysis

To assess suitability for our proposed method, we analyze memory and computational costs as well as sources of errors of Baker's iSVD and SketchySVD, comparing them to standard batch SVD in Table 1.

Baker's method has space complexity $O(nr)$ for storing \mathbf{V}_r , making it suitable for large-scale problems where $n \gg r$ and $r < K$. The per-iteration cost of $O(nr)$ yields total complexity $O(nKr)$, matching batch SVD. However, error characteristics differ fundamentally. While batch SVD error stems solely from truncating small singular values [96], Baker's iSVD introduces incremental error accumulating with each update. Denoting the final iSVD approximation as $\tilde{\mathbf{X}}_{\text{isvd}} = \tilde{\mathbf{V}}\tilde{\Sigma}\tilde{\mathbf{W}}^\top$ corresponding to time step $k = K$ versus the batch result $\mathbf{X} = \mathbf{V}\Sigma\mathbf{W}^\top$, there exists a bound $\varepsilon > 0$ satisfying $\|\mathbf{X} - \tilde{\mathbf{X}}_{\text{isvd}}\|_2 \leq \varepsilon$ [97]. This bound implies singular value perturbations $|\sigma_j - \tilde{\sigma}_j| \leq \varepsilon$ between diagonal entries of Σ and $\tilde{\Sigma}$, while singular vector errors depend on spectral gaps between consecutive singular values. Notably, right singular vectors exhibit larger errors than left vectors [97, Thm. 3.9]:

$$\|\mathbf{v}_j - \tilde{\mathbf{v}}_j\|_2 \leq E_j^{1/2}, \quad \|\mathbf{w}_j - \tilde{\mathbf{w}}_j\|_2 \leq E_j^{1/2} + 2\sigma_j^{-1}\varepsilon_j, \quad (10)$$

where $\mathbf{v}_j, \mathbf{w}_j$ (resp. $\tilde{\mathbf{v}}_j, \tilde{\mathbf{w}}_j$) denote the j -th left and right singular vectors of \mathbf{V}, \mathbf{W} (resp. $\tilde{\mathbf{V}}, \tilde{\mathbf{W}}$), and $E_j, \varepsilon_j > 0$ depend on ε , singular values, and their gaps. Errors in both vectors increase as $\sigma_j \rightarrow 0$ due to diminishing spectral gaps, which can be mitigated by choosing smaller r to focus on dominant modes. For more details, see [97].

SketchySVD memory requirements are dominated by the dense range sketch X_{range} at $O(nq)$, with smaller corange and core sketches requiring $O(qK)$ and $O(s^2)$. The sparse sign matrix draws each column of the reduction maps independently from a distribution where each entry is $+1$ or -1 with probability based on $\zeta = \min\{q, 8\}$, a sparsity parameter controlling the number of nonzeros per column, adding $O(n\zeta)$ memory [67]. Total memory of $O(n(q + \zeta) + qK + s^2)$ remains well below the $O(nK)$ needed for full data if $q, s \ll n$ and $q, s < K$. The per-iteration cost of $O(n\zeta)$ for three sparse matrix-vector multiplications yields total complexity $O(nK\zeta)$, proportional to the large-scale dimension n . Unlike Baker's deterministic accumulation, SketchySVD errors are probabilistic. For sketch parameters q and s , the expected Frobenius error between \mathbf{X} and its approximation $\tilde{\mathbf{X}}_{\text{sketchy}}$ satisfies [67, Thm. 5.1]

$$\mathbb{E}\|\mathbf{X} - \tilde{\mathbf{X}}_{\text{sketchy}}\|_F^2 \leq \frac{s-1}{s-q-1} \cdot \min_{\varrho < q-1} \frac{q+\varrho-1}{q-\varrho-1} \cdot \sum_{j>q+1} \sigma_j^2, \quad (11)$$

where the tail energy $\sum_{j>q+1} \sigma_j^2$ reveals SketchySVD's ability to exploit spectral decay. That is, increasing q captures more spectrum, reducing tail energy. Similar to Baker's method, errors grow with smaller spectral gaps, particularly pronounced in turbulent and advection-dominant flows with slow spectral decay. Such problems require larger q and s for accuracy, increasing memory usage.

The choice between methods depends on memory constraints, accuracy requirements, and spectral decay rates. Baker's iSVD offers minimal memory overhead, ideal for problems with fast spectral decay and modest datasets. SketchySVD trades increased memory for better scalability to large datasets, with tunable sketch sizes balancing accuracy and storage. Section 4 demonstrates effective integration of both methods within our streaming OpInf framework across different problem types.

Table 1: Summary of memory and computational costs as well as sources of errors of the standard batch SVD, Baker's iSVD, and SketchySVD algorithms for computing a rank- r truncated SVD of a data matrix $\mathbf{X} \in \mathbb{R}^{n \times K}$. Here, q and s are the sketch sizes in SketchySVD such that $r < q \leq s$, and $\zeta = \min\{q, 8\}$ is the sparsity parameter for the sparse sign matrices used as reduction maps.

Algorithm	Memory Cost	Time Cost	Source of Error
Standard Batch SVD	$O(n(K+r))$	$O(nKr)$	Truncation error based on r [96]
Baker's iSVD [66]	$O(nr)$	$O(nKr)$	Truncation error and spectral gap [97]
SketchySVD [67]	$O(n(q+\zeta))$	$O(nK\zeta)$	Error bound based on r, q, s [67]

2.3. Recursive Least-Squares Methods

We introduce two RLS algorithms: standard RLS and a more numerically stable incremental QR-decomposition Recursive Least Squares (iQRRLS) in Sections 2.3 and 2.3.2.

2.3.1. Standard RLS Algorithm

We consider a streaming setting in which the rows of the OpInf least squares problem become available sequentially. At each step k , new streaming data arrives as $(\mathbf{d}_k, \mathbf{r}_k)$, where $\mathbf{d}_k \in \mathbb{R}^{1 \times d}$ represents the final row from the current data matrix $\mathbf{D}_k = [\mathbf{d}_1; \mathbf{d}_2; \dots; \mathbf{d}_k] \in \mathbb{R}^{k \times d}$ and $\mathbf{r}_k \in \mathbb{R}^{1 \times r}$ is the corresponding final row from $\mathbf{R}_k = [\mathbf{r}_1; \mathbf{r}_2; \dots; \mathbf{r}_k] \in \mathbb{R}^{k \times r}$. The streams \mathbf{d}_k and \mathbf{r}_k are formed by reduced snapshots $\hat{\mathbf{x}}_k$ and $\hat{\mathbf{x}}_k$ as defined in (5). To develop the RLS formulation, consider the normal equation solution to (4), which gives the operator solution \mathbf{O}_k at step k :

$$\mathbf{O}_k = \mathbf{P}_k \mathbf{D}_k^\top \mathbf{R}_k \quad \text{where} \quad \mathbf{P}_k = (\mathbf{D}_k^\top \mathbf{D}_k + \boldsymbol{\Gamma})^{-1},$$

and $\mathbf{P}_k \in \mathbb{R}^{d \times d}$ is the *inverse correlation matrix* at step k . In RLS, the inverse \mathbf{P}_k^{-1} is updated recursively as

$$\mathbf{P}_k^{-1} = \mathbf{P}_{k-1}^{-1} + \mathbf{d}_k^\top \mathbf{d}_k = \mathbf{P}_0^{-1} + \sum_{i=1}^k \mathbf{d}_i^\top \mathbf{d}_i, \quad k = 1, 2, \dots, K,$$

initialized with $\mathbf{P}_0^{-1} = \boldsymbol{\Gamma}$. The inclusion of the Tikhonov regularization term $\boldsymbol{\Gamma}$ is critical, since the RLS algorithm consists of many rank-1 updates that are prone to ill-conditioning without regularization.

The key insight of RLS is to efficiently update the inverse correlation matrix \mathbf{P}_k using the Sherman-Morrison identity, which enables rank-1 updates without recomputing the entire matrix inverse [68]. This approach transforms the $O(d^3)$ matrix inversion into $O(d^2)$ operations per iteration. The RLS algorithm hence becomes an update of the LS solution by adding a correction term based on the prediction error:

$$\mathbf{O}_k = \mathbf{O}_{k-1} + \mathbf{g}_k \boldsymbol{\xi}_k^-, \quad (12)$$

where $\boldsymbol{\xi}_k^- = \mathbf{r}_k - \mathbf{d}_k \mathbf{O}_{k-1} \in \mathbb{R}^{1 \times r}$ is the *a priori* prediction error and $\mathbf{g}_k = \mathbf{P}_{k-1} \mathbf{d}_k^\top c_k \in \mathbb{R}^d$ is called the Kalman gain vector with conversion factor $c_k > 0$ [68]. Both the conversion factor and the inverse correlation matrix are also updated recursively using the new data. RLS is initialized with $\mathbf{O}_0 = \mathbf{0}_{d \times r}$ and repeats the update (12) as well as the updates for c_k and \mathbf{P}_k for each new data stream $(\mathbf{d}_k, \mathbf{r}_k)$ until all K data points are processed to yield the final operator estimate \mathbf{O}_K . The RLS algorithm is summarized in Algorithm 3.

2.3.2. Inverse QR-Decomposition RLS Algorithm

While the standard RLS algorithm 3 is effective for recursive parameter estimation, it suffers from numerical instabilities when updating the inverse correlation matrix \mathbf{P}_k in finite-precision arithmetic. These instabilities arise because updating \mathbf{P}_k involves subtracting two positive definite matrices, which can destroy positive definiteness and cause *catastrophic cancellation* when nearly equal large values are subtracted [68]. To address these numerical instabilities, QR-decomposition RLS algorithms organize iterated quantities and incoming data into arrays that are factorized using QR decomposition to update the necessary variables in a numerically stable manner.

These algorithms rely on transformations of the form $\mathcal{A}_k \boldsymbol{\Theta}_k = \mathcal{B}_k$, where \mathcal{A}_k is the *pre-array* containing previous quantities and new data, $\boldsymbol{\Theta}_k$ is a unitary matrix (e.g., a product of Givens rotations or Householder reflections), and \mathcal{B}_k is the triangular *post-array* containing updated quantities. This transformation is essentially a QR decomposition of \mathcal{A}_k^\top , leading to two main variants: iQRRLS and QR-decomposition Recursive Least Squares (QRRLS), which differ in whether they update the inverse correlation matrix \mathbf{P}_k or the correlation matrix $\sum_{i=1}^k \mathbf{d}_i^\top \mathbf{d}_i$ [68, 69].

The iQRRLS algorithm specifically addresses numerical instability by propagating the square root of the inverse correlation matrix $\mathbf{P}_k^{1/2}$ rather than \mathbf{P}_k itself to ensure positive definiteness, using the Cholesky decomposition $\mathbf{P}_k = \mathbf{P}_k^{1/2} (\mathbf{P}_k^{1/2})^\top$ where $\mathbf{P}_k^{1/2}$ is lower triangular. iQRRLS then organizes the transposed square root matrix from the previous iteration, denoted with shorthand notation $\mathbf{P}_{k-1}^{1/2} = (\mathbf{P}_{k-1}^{1/2})^\top$, and incoming data into the pre-array

$$\mathcal{A}_k^\top = \begin{bmatrix} 1 & \mathbf{0}_{1 \times d} \\ \mathbf{P}_{k-1}^{\top/2} \mathbf{d}_k^\top & \mathbf{P}_{k-1}^{\top/2} \end{bmatrix} \in \mathbb{R}^{(d+1) \times (d+1)},$$

and then performs QR decomposition to obtain the post-array from which updated quantities can be extracted:

$$c_k^{-1/2} \leftarrow \mathcal{B}_k^\top (1, 1), \quad \mathbf{g}_k c_k^{-1/2} \leftarrow \mathcal{B}_k^\top (1, 2 : d+1), \quad \mathbf{P}_k^{1/2} \leftarrow (\mathcal{B}_k^\top (2 : d+1, 2 : d+1))^\top,$$

where (i, j) denotes the matrix entry at row i and column j . We summarize iQRRLS in Algorithm 4.

2.3.3. Cost Analysis

To assess the computational efficiency of RLS methods for streaming OpInf, we present their memory and computational costs, comparing them to standard batch LS in Table 2. A key advantage of RLS methods is their constant memory requirement of $O(d^2)$, dominated by storing the inverse correlation matrix $\mathbf{P}_k \in \mathbb{R}^{d \times d}$, compared to the $O(d(K + d))$ storage required by batch LS for the concatenated data matrix $\bar{\mathbf{D}}$. In the standard RLS algorithm, each iteration requires $O(d^2)$ operations for updating \mathbf{P}_k and computing the Kalman gain, yielding a total cost of $O(Kd^2)$ for processing K data points, which is comparable to the $O(d^2 \max\{K, d\})$ cost of batch LS solutions [68]. Unlike batch methods, RLS does not require storing the entire data history, making it well-suited for streaming applications.

The iQRRLS algorithm addresses numerical stability by propagating the Cholesky factor $\mathbf{P}_k^{\top/2}$ (an upper triangular matrix) instead of the full inverse correlation matrix. At each iteration, iQRRLS performs a QR decomposition of a $(d + 1) \times (d + 1)$ pre-array matrix \mathcal{A}_k^\top . A naïve implementation would require $O(d^3)$ operations per iteration. However, because $\mathbf{P}_k^{\top/2}$ is upper triangular, \mathcal{A}_k^\top has a nearly upper triangular structure, allowing Givens rotations to be applied selectively to only the first column. This reduces the computational complexity to $O(d^2)$ per iteration [68], matching standard RLS asymptotically. For dimensions below 20, the computational difference is negligible, but Givens rotations become essential for larger problems. Moreover, the memory cost of iQRRLS can be half of the standard RLS if we opt to store only the upper triangular elements of $\mathbf{P}_k^{\top/2}$.

The QRRLS algorithm similarly addresses numerical instability by propagating the Cholesky factor of the correlation matrix $\sum_{i=1}^k \mathbf{d}_k^\top \mathbf{d}_k$ instead of its inverse. However, a key difference is that QRRLS requires an additional LS solve at each iteration after extracting the updated quantities from the post-array to compute the operator estimate \mathbf{O}_k . This incurs an additional cost per iteration, and thus, we consider iQRRLS as our primary array-based RLS method in this work. For more details on both iQRRLS and QRRLS, see [68].

Table 2: Summary of memory and computational costs of standard LS, standard RLS, and iQRRLS algorithms for solving the regularized LS problem (4) with K data points and d features.

Algorithm	Memory Cost	Time Cost
Standard Batch LS	$O(d(K + d))$	$O(d^2 \max\{K, d\})$
Standard RLS [68]	$O(d^2)$	$O(Kd^2)$
iQRRLS [68]	$O(d^2)$	$O(Kd^2)$

3. Streaming Operator Inference for Large-Scale Data

In this section, we present Streaming OpInf, a reduced operator learning method that extends the OpInf framework to the data-streaming setting. In Section 3.1, we detail the mathematical reformulation of the learning step for Streaming OpInf. In Section 3.2, we provide guidance on selecting appropriate algorithmic components based on problem characteristics. In Section 3.3, we analyze the sources of error in Streaming OpInf. Finally, in Section 3.4, we provide practical implementation details.

3.1. Streaming Reformulation of the Learning Step

Adapting the standard OpInf framework (4) to the data-streaming setting requires replacing the batch SVD and LS computations with their streaming counterparts from Sections 2.2 and 2.3. A straightforward approach would be to first compute the POD basis via iSVD, then make an additional pass through the data to project each snapshot and its time derivative onto this basis, and finally solve for the operators using either batch LS or RLS. We refer to this as the *projection* approach, which yields the *iSVD-Project-LS* and *iSVD-Project-RLS* paradigms. However, this projection step incurs a computational cost of $O(nr)$ per snapshot—totaling $O(nKr)$ for K snapshots—which can be prohibitive when n is extremely large.

To circumvent this additional data pass and its associated cost, we introduce a reformulation that expresses the LS data matrices directly in terms of the truncated SVD matrices obtained from iSVD, thereby avoiding explicit projection entirely. This *reformulation* approach yields the *iSVD-LS* and *iSVD-RLS* paradigms.

Specifically, suppose streamed snapshots $\mathbf{X}_k = [\mathbf{x}_1, \dots, \mathbf{x}_k] \in \mathbb{R}^{n \times k}$ have been processed by iSVD up to time step k , yielding a rank- r_k truncated SVD approximation $\hat{\mathbf{X}}_k \approx \mathbf{V}_{r_k} \boldsymbol{\Sigma}_{r_k} \mathbf{W}_{r_k}^\top$ with $r_k \leq r$. The reduced snapshot matrix can then be expressed as

$$\hat{\mathbf{X}}_k = \mathbf{V}_{r_k}^\top \mathbf{X}_k = \boldsymbol{\Sigma}_{r_k} \mathbf{W}_{r_k}^\top, \quad (13)$$

where each row corresponds to a right singular vector scaled by its singular value. For quadratic terms, we employ properties of the Kronecker product [98] and Khatri-Rao product [99, 100] to obtain

$$\begin{aligned} \mathbf{X}_k \odot \mathbf{X}_k &\approx (\mathbf{V}_{r_k} \otimes \mathbf{V}_{r_k})(\boldsymbol{\Sigma}_{r_k} \otimes \boldsymbol{\Sigma}_{r_k})(\mathbf{W}_{r_k} \ominus \mathbf{W}_{r_k})^\top \\ \implies \hat{\mathbf{X}}_k \odot \hat{\mathbf{X}}_k &= (\boldsymbol{\Sigma}_{r_k} \otimes \boldsymbol{\Sigma}_{r_k})(\mathbf{W}_{r_k} \ominus \mathbf{W}_{r_k})^\top = \boldsymbol{\Sigma}_{r_k} \mathbf{W}_{r_k}^\top \odot \boldsymbol{\Sigma}_{r_k} \mathbf{W}_{r_k}^\top, \end{aligned} \quad (14)$$

where \ominus denotes the row-wise Kronecker product (also known as the face-splitting product [101]), and we use $(\mathbf{V}_{r_k} \otimes \mathbf{V}_{r_k})^\top (\mathbf{V}_{r_k} \otimes \mathbf{V}_{r_k}) = \mathbf{I}_{r_k^2}$.

Using (13) and (14), the data matrix \mathbf{D}_k from (5) can be reformulated solely in terms of the rank- r truncated matrices $\boldsymbol{\Sigma}_r = \boldsymbol{\Sigma}_{r_k}(1:r, 1:r)$ and $\mathbf{W}_r = \mathbf{W}_{r_k}(:, 1:r)$:

$$\mathbf{D}_k = [\mathbf{W}_r \boldsymbol{\Sigma}_r \quad \mathbf{W}_r \boldsymbol{\Sigma}_r \ominus \mathbf{W}_r \boldsymbol{\Sigma}_r \quad \mathbf{U}_k^\top \quad \mathbf{1}_k],$$

noting that $\mathbf{W}_r \boldsymbol{\Sigma}_r \ominus \mathbf{W}_r \boldsymbol{\Sigma}_r = \boldsymbol{\Sigma}_r \mathbf{W}_r^\top \odot \boldsymbol{\Sigma}_r \mathbf{W}_r^\top$ since the Khatri-Rao product equals the transposed face-splitting product.

The right-hand side matrix \mathbf{R}_k can similarly be expressed using $\boldsymbol{\Sigma}_r$ and \mathbf{W}_r when time derivatives are approximated via finite differences. Denoting the finite difference operator matrix as $\Delta_k \in \mathbb{R}^{k \times \bar{k}}$, where $\bar{k} \leq k$ depends on the chosen scheme, the reduced time derivative matrix becomes $\dot{\hat{\mathbf{X}}}_k = \boldsymbol{\Sigma}_r \mathbf{W}_r^\top \Delta_k$, and thus $\mathbf{R}_k = \Delta_k^\top \mathbf{W}_r \boldsymbol{\Sigma}_r$. For example, forward differences with constant time step δt yield

$$\Delta_k = \frac{1}{\delta t} \begin{bmatrix} -1 & 0 & 0 & \cdots & 0 \\ 1 & -1 & 0 & \cdots & 0 \\ 0 & 1 & -1 & \cdots & 0 \\ \vdots & & \vdots & \ddots & \vdots \\ 0 & \cdots & 0 & 1 & -1 \\ 0 & \cdots & 0 & 0 & 1 \end{bmatrix} \in \mathbb{R}^{k \times (k-1)}.$$

Since finite differencing can change the column dimension from k to \bar{k} , a column selector matrix $\mathbf{S}_k \in \mathbb{R}^{k \times \bar{k}}$ extracts the appropriate indices from the snapshot data (e.g., indices 1 to $k-1$ for forward differences). The final formulation with Tikhonov regularization becomes

$$\bar{\mathbf{D}}_k = \begin{bmatrix} \mathbf{S}_k^\top \mathbf{W}_r \boldsymbol{\Sigma}_r & \mathbf{S}_k^\top \mathbf{W}_r \boldsymbol{\Sigma}_r \ominus \mathbf{S}_k^\top \mathbf{W}_r \boldsymbol{\Sigma}_r & \mathbf{S}_k^\top \mathbf{U}_k^\top & \mathbf{1}_{\bar{k}} \\ \mathbf{I}^{1/2} & & & \end{bmatrix}, \quad \bar{\mathbf{R}}_k = \begin{bmatrix} \Delta_k^\top \mathbf{W}_r \boldsymbol{\Sigma}_r \\ \mathbf{0}_{d \times r} \end{bmatrix}. \quad (15)$$

This reformulation offers two key advantages. First, it computes the data matrices $\bar{\mathbf{D}}_k$ and $\bar{\mathbf{R}}_k$ directly from the iSVD output without storing more than one snapshot at a time. Second, it avoids explicit projection of \mathbf{X}_k onto the POD basis, eliminating the $O(nKr)$ computational overhead of the projection step. The operator solution $\mathbf{O}_k = \bar{\mathbf{D}}_k^\dagger \bar{\mathbf{R}}_k$ can then be computed at any time step k using only the data processed thus far, enabling online operator learning with the potential for real-time predictions.

3.2. Streaming Paradigms and Algorithm Selection

As summarized in Figure 1 and Table 3, we thoroughly explore the design space of Streaming OpInf and propose four distinct paradigms—*iSVD-Project-LS*, *iSVD-Project-RLS*, *iSVD-LS*, and *iSVD-RLS*—distinguished by two independent design choices: (i) whether time derivative data is available directly or must be approximated via finite differences, and (ii) whether to solve the LS problem in batch or recursively.

The first design choice concerns how the reduced time derivative data is obtained. When time derivative data is unavailable or unreliable (e.g., corrupted by measurement noise), the reformulation (15) approximates derivatives via finite differences applied directly to the iSVD output, yielding the iSVD-LS/RLS paradigms. This approach avoids

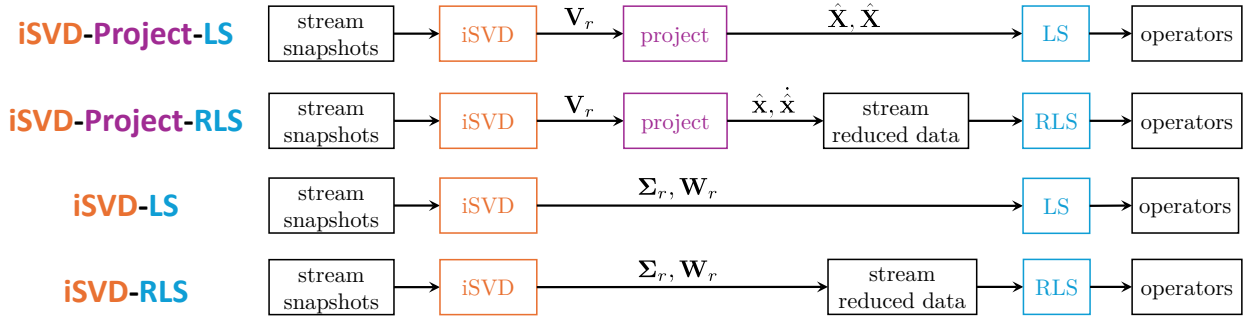


Figure 1: Flowchart of each paradigm of Streaming OpInf showing different algorithmic components, selected based on time derivative data availability and memory/computational cost considerations.

the computational cost of projecting data onto the POD basis. Conversely, when high-quality time derivative data is available from simulations or experiments, it can be projected onto the POD basis after computing the basis via iSVD. This projection approach, yielding the iSVD-Project-LS/RLS paradigms, avoids the potential inaccuracies of finite difference approximations and is generally preferred when accurate derivative data is accessible. However, it requires an additional pass through the data with a total cost of $O(2nKr)$ for projecting both snapshots and derivatives. This cost is often manageable through parallelized batch processing, though it may be prohibitive for extremely large n or when data cannot be revisited.

The second design choice concerns how the linear LS problem is solved. In the iSVD-LS and iSVD-Project-LS paradigms, the operator is computed via batch LS using the data matrices from (15) or (5), respectively. For iSVD-LS, this approach enables computation of the operator at any intermediate time step k , which may be valuable for applications requiring online operator estimates. Alternatively, the iSVD-RLS and iSVD-Project-RLS paradigms employ the RLS methods from Section 2.3. iSVD-RLS streams $\hat{\mathbf{x}}_k = \Sigma_r \mathbf{W}_r^\top(:, k)$, with time derivatives approximated using finite differences over a sliding window while iSVD-Project-RLS projects streams $\{\hat{\mathbf{x}}, \dot{\hat{\mathbf{x}}}\}$. Unlike the batch approaches, the RLS paradigms yield the operator only after processing all K snapshots, since RLS updates commence after iSVD completion. However, this approach requires only $O(d^2)$ additional memory compared to $O(d(K + d))$ for the batch paradigms (see Table 3), making it more memory-efficient and fully streaming without batch computations.

Table 3: Summary of memory and computational costs for Streaming OpInf paradigms. Here, n is the full system dimension, K is the number of snapshots, r is the reduced basis dimension, $d = r + r^2 + m + 1$ is the total operator dimension, m is the input dimension, $r < q$, s are SketchySVD sketch sizes, and $\zeta = \min\{q, 8\}$ is the sparsity parameter.

Streaming OpInf	iSVD Method	Memory Cost	Computational Cost
iSVD-LS	Baker's iSVD	$O(nr + d(K + d))$	$O(nKr + d^2 \max\{d, K\})$
	SketchySVD	$O(n(q + \zeta) + d(K + d))$	$O(nK\zeta + d^2 \max\{d, K\})$
iSVD-RLS	Baker's iSVD	$O(nr + d^2)$	$O(nKr + Kd^2)$
	SketchySVD	$O(n(q + \zeta) + d^2)$	$O(nK\zeta + Kd^2)$
iSVD-Project-LS	Baker's iSVD	$O(nr + d(K + d))$	$O(3nKr + d^2 \max\{d, K\})$
	SketchySVD	$O(n(q + \zeta) + d(K + d))$	$O(nK(\zeta + 2r) + d^2 \max\{d, K\})$
iSVD-Project-RLS	Baker's iSVD	$O(nr + d^2)$	$O(3nKr + Kd^2)$
	SketchySVD	$O(n(q + \zeta) + d^2)$	$O(nK(\zeta + 2r) + Kd^2)$

To summarize, practitioners should select among the four paradigms based on the following considerations: (i) use projection paradigms (iSVD-Project-LS/RLS) when accurate derivative data is available and the $O(2nKr)$ projection cost is acceptable, and reformulation paradigms (iSVD-LS/RLS) otherwise; (ii) use the iSVD-LS paradigm when intermediate operator solutions at time $k < K$ are needed for possibly real-time scenarios; and (iii) use RLS paradigms (iSVD-RLS or iSVD-Project-RLS) when memory is limited and K is large, as they require only $O(d^2)$ additional stor-

age. Additional practical considerations such as implementation complexity, numerical stability, and computational infrastructure may also influence the choice in specific application contexts. Moreover, other paradigms, for example, hybrid approaches which combine iSVD-LS/RLS by computing a sufficiently accurate POD basis up to time $k' < K$ using a subset of the data and then performing projection and RLS updates for $k > k'$, can also be devised within the Streaming OpInf framework to suit particular needs.

3.3. Sources of Error

Streaming OpInf introduces approximation errors relative to batch OpInf from two sources: (i) errors in the POD basis from streaming SVD methods, and (ii) errors in the operator solution from using RLS instead of batch LS. We analyze each source in this section.

3.3.1. Errors from Streaming SVD

Baker's iSVD produces deterministic errors that accumulate with each truncation [66, 97], while SketchySVD produces probabilistic errors controlled by sketch parameters [67]. Both methods exhibit increased errors when spectral gaps diminish, as discussed in Section 2.2.3. These errors propagate to the learned operators through the LS data matrices. Specifically, the iSVD-LS/RLS paradigms construct data matrices (15) using right singular vectors \mathbf{W}_r and singular values Σ_r , which carry larger errors than left singular vectors according to (10). In contrast, the iSVD-Project-LS/RLS paradigms project data onto the POD basis using left singular vectors \mathbf{V}_r , yielding lower operator error at additional computational cost. We formalize this error propagation in the following lemmas and theorem.

The first lemma establishes a general perturbation bound for the learned operators in terms of perturbations to the data matrices.

Lemma 3.1 (Operator perturbation bound). *Let $\tilde{\mathbf{D}} = \bar{\mathbf{D}} + [\mathbf{E}_D^\top, \mathbf{0}_{d \times d}]^\top$ and $\tilde{\mathbf{R}} = \bar{\mathbf{R}} + [\mathbf{E}_R^\top, \mathbf{0}_{r \times d}]^\top$ denote perturbed versions, where the perturbations $\mathbf{E}_D \in \mathbb{R}^{K \times d}$ and $\mathbf{E}_R \in \mathbb{R}^{K \times r}$ arise from approximate SVD factors. Then the operator error between the batch solution $\mathbf{O} = \bar{\mathbf{D}}^\dagger \bar{\mathbf{R}}$ and the streaming solution $\tilde{\mathbf{O}} = \tilde{\mathbf{D}}^\dagger \tilde{\mathbf{R}}$ satisfies*

$$\|\mathbf{O} - \tilde{\mathbf{O}}\|_F \leq \alpha \|\bar{\mathbf{D}}^\dagger\|_2 \|\tilde{\mathbf{D}}^\dagger\|_2 \|\mathbf{E}_D\|_2 \|\bar{\mathbf{R}}\|_F + \|\bar{\mathbf{D}}^\dagger\|_2 \|\mathbf{E}_R\|_F, \quad (16)$$

where $\alpha = \sqrt{2}$ if $K \neq d$ and $\alpha = 1$ if $K = d$.

The second lemma bounds the data matrix perturbations \mathbf{E}_D and \mathbf{E}_R in terms of the singular vector and singular value errors from streaming SVD. Let $\{\mathbf{v}_j, \sigma_j, \mathbf{w}_j\}_{j=1}^r$ and $\{\tilde{\mathbf{v}}_j, \tilde{\sigma}_j, \tilde{\mathbf{w}}_j\}_{j=1}^r$ denote the singular triplets from exact and approximate rank- r SVD, respectively, where the singular vectors are orthonormal.

Lemma 3.2 (Data matrix perturbation bounds). *Let $\bar{\mathbf{D}}$ and $\bar{\mathbf{R}}$ be constructed using the exact rank- r SVD of \mathbf{X} , and let $\tilde{\mathbf{D}}$ and $\tilde{\mathbf{R}}$ be constructed using approximate factors $\tilde{\mathbf{V}}_r, \tilde{\Sigma}_r, \tilde{\mathbf{W}}_r$ from streaming SVD. Assume the time-derivative data is computed via finite differences, i.e., $\dot{\mathbf{X}} = \mathbf{X} \Delta_K$. Suppose $\|\mathbf{X} - \tilde{\mathbf{X}}\|_2 \leq \varepsilon$, which implies $|\sigma_j - \tilde{\sigma}_j| \leq \varepsilon$ for all $j = 1, \dots, r$. Let $\|\mathbf{v}_j - \tilde{\mathbf{v}}_j\|_2 \leq \varepsilon_{v,j}$ and $\|\mathbf{w}_j - \tilde{\mathbf{w}}_j\|_2 \leq \varepsilon_{w,j}$ for all j . Define the cumulative singular vector errors*

$$\tau_v = \left(\sum_{j=1}^r \varepsilon_{v,j}^2 \right)^{1/2}, \quad \tau_w = \left(\sum_{j=1}^r \varepsilon_{w,j}^2 \right)^{1/2}. \quad (17)$$

Then for the iSVD-Project-LS/RLS paradigms (projection onto POD basis),

$$\|\mathbf{E}_D\|_2 \leq \frac{\beta_1}{\sqrt{\min\{n, K\}}} \tau_v, \quad \|\mathbf{E}_R\|_F \leq \sigma_1 \|\Delta_K\|_2 \tau_v. \quad (18)$$

For the iSVD-LS/RLS paradigms (reformulation (15)),

$$\|\mathbf{E}_D\|_2 \leq \frac{\sigma_1 \beta_2}{\sqrt{r}(\sigma_1 + \varepsilon)} \tau_w + \frac{\beta_2}{\sigma_1 + \varepsilon} \varepsilon, \quad \|\mathbf{E}_R\|_F \leq \sigma_1 \|\Delta_K\|_2 \tau_w + \sqrt{r} \|\Delta_K\|_2 \varepsilon. \quad (19)$$

Constants $\beta_1, \beta_2 > 0$ depend on σ_1 , bound of \mathbf{U} , and dimension K where σ_1 denotes the largest singular value of \mathbf{X} .

Combining these lemmas yields the main result, bounding the operator error for each paradigm.

Theorem 3.3 (Operator error bounds). *Suppose $\Gamma = \text{diag}(\gamma_1, \dots, \gamma_d)$ with $\gamma_j > 0$ for all j , and assume that $\sqrt{\gamma_{\min}} = \min_j \sqrt{\gamma_j} \gg \sigma_{\min}(\mathbf{D}), \sigma_{\min}(\mathbf{D} + \mathbf{E}_D)$. Under the assumptions of Lemma 3.2, the operator error in Lemma 3.1 satisfies the following bounds. For the iSVD-Project-LS/RLS paradigms,*

$$\|\mathbf{O} - \widetilde{\mathbf{O}}\|_F \leq \frac{\sigma_1 \|\Delta_K\|_2}{\sqrt{\gamma_{\min}}} \tau_v \left(1 + \frac{\alpha \beta_1}{\sqrt{\gamma_{\min}}}\right). \quad (20)$$

For the iSVD-LS/RLS paradigms,

$$\|\mathbf{O} - \widetilde{\mathbf{O}}\|_F \leq \frac{\sigma_1 \|\Delta_K\|_2}{\sqrt{\gamma_{\min}}} \tau_w \left(1 + \frac{\alpha \beta_2}{\sqrt{\gamma_{\min}}}\right) + \frac{(\alpha \beta_2 + \sqrt{\gamma_{\min}}) \sqrt{r} \|\Delta_K\|_2}{\gamma_{\min}} \varepsilon. \quad (21)$$

These theoretical results yield two key observations. First, when $\varepsilon_{w,j} > \varepsilon_{v,j}$ for all j , as is the case for iSVD algorithms satisfying (10), the iSVD-Project-LS/RLS paradigms can yield lower operator error than iSVD-LS/RLS. This follows because the bound (21) depends on τ_w and includes additional terms in ε , whereas the bound (20) depends only on τ_v . Thus, projection paradigms are preferable when operator accuracy is critical and the additional computational cost and data passes are acceptable.

Second, when the spectral decay is slow (e.g., the turbulent channel flow example in Section 4.3), the errors $\varepsilon_{w,j}$, $\varepsilon_{v,j}$, and ε increase due to an insufficient reduced rank r to capture the dominant modes. In such cases, increasing the regularization parameter γ_{\min} can mitigate operator error by reducing sensitivity to these perturbations. For proofs of Lemmas 3.1 and 3.2 and theorem 3.3, see Appendix C.

3.3.2. Errors from Recursive Least Squares

When using RLS instead of batch LS, an additional source of error arises from the recursive updates. We define the *streaming operator error* (SOE) as the difference between the RLS solution \mathbf{O}_k at time step k and the batch LS solution \mathbf{O} obtained using all available data:

$$\text{SOE}(k) = \mathbf{O} - \mathbf{O}_k = \text{SOE}(k-1) - \mathbf{g}_k \xi_k^-, \quad (22)$$

following a recursive update analogous to (12). Assessing this error is important when considering RLS over batch LS, as it reveals the accuracy trade-offs introduced by the recursive updates.

The convergence of $\text{SOE}(k) \rightarrow 0$ as $k \rightarrow K$ indicates that the RLS algorithm effectively approximates the batch solution as more data is processed. In noise-free scenarios, $\text{SOE}(k)$ converges to zero exactly. In the presence of noise, $\text{SOE}(k)$ may not vanish but should decrease in a mean-square sense, reflecting the algorithm's ability to learn the underlying operators despite measurement noise [102, p. 21].

Overall, the total operator error in the iSVD-LS and iSVD-Project-LS frameworks is due solely to errors from streaming SVD defined in Theorem 3.3. In contrast, the total operator error in iSVD-RLS and iSVD-Project-RLS frameworks is a combination of errors from streaming SVD defined in Theorem 3.3 and errors from RLS updates (22), in which the RLS solution approaches $\widetilde{\mathbf{O}}$ solved using matrices from streaming SVD with batch LS. In Section 4, we assess the streaming operator error to evaluate the convergence behavior of the RLS algorithms in practice.

3.4. Practical Considerations

The operator inference problem is formulated as a linear LS problem where conditioning critically affects operator quality and stability. Linear and polynomial state dependencies due to small time step δt yield high condition numbers, compounded by noise from numerical time-derivative approximation, model misspecification, and unresolved dynamics from POD truncation [55].

To improve conditioning, Streaming OpInf applies preprocessing to snapshot data: mean-centering ensures the POD basis captures dominant variation modes [103], while min-max normalization (e.g., scaling to $[0, 1]$ or $[-1, 1]$) prevents bias toward larger-magnitude variables in multi-physics systems [2, 8]. This is crucial for turbulent channel flow (Section 4.3), where streamwise velocity dominates. When making predictions, these transformations are inverted to return solutions in physical coordinates. Computing mean and min-max values requires an additional data pass, efficiently handled via batch processing and parallelization.

The initialization of \mathbf{P}_0 (see Algorithms 3 and 4) avoids impractical initialization of $\mathbf{D}_k^\top \mathbf{D}_k$ as $\infty \cdot \mathbf{I}_d$ at $k = 0$, which suppresses the solution to zero [68, p. 495]. This initialization also provides regularization, with the common choice $\mathbf{P}_0 = \gamma^{-1} \mathbf{I}_d$ for small $\gamma > 0$ corresponding to Tikhonov regularization [102, p. 20]. We use $\gamma = 1 \times 10^{-9}$, which yielded stable models in our benchmark experiments. Since RLS algorithms suffer from ill-conditioning of the inverse correlation matrix with many rank-1 updates (or equivalently, small window sizes), this regularization is crucial for numerical stability [104].

For large-scale problems, optimal regularization balancing training error and long-time stability is critical. Following [8], we employ $\mathbf{\Gamma} = \text{diag}(\gamma_1 \mathbf{I}_{d_1}, \gamma_2 \mathbf{I}_{d_2})$, where $\gamma_1 > 0$ acts on linear and constant terms and $\gamma_2 > 0$ on quadratic terms, with $d_1 = r + m + 1$, $d_2 = r^2$, and $d = d_1 + d_2$. We select γ_1, γ_2 via grid search, evaluating state prediction error of the inferred model over a validation dataset for each parameter pair.

4. Numerical Experiments

In this section, we present numerical experiments to evaluate the performance of the proposed Streaming OpInf method across different Streaming OpInf paradigms as defined in Section 3.2. We consider three distinct problems: (i) one-dimensional viscous Burgers' Equation (Section 4.1), (ii) Kuramoto-Sivashinsky Equation (KSE) (Section 4.2), and (iii) three-dimensional turbulent channel flow (Section 4.3).

The first two experiments are conducted on a desktop machine with 128GB of memory. The iSVD phase of the channel flow problem was performed on the National Laboratory of the Rockies (NLR) high-performance computing cluster, Kestrel, using a single node with 300GB of allocated memory, while the LS phase was performed on the desktop machine. The experiment codes are publicly available for reproducibility¹.

4.1. Viscous Burgers' Equation

Our first numerical experiment uses a benchmark model reduction problem based on the one-dimensional viscous Burgers' equation, a simplified fluid dynamics model describing the motion of a one-dimensional viscous fluid [1, 17, 23, 105]. Despite this problem being a small example which can be handled by standard batch OpInf, it serves as a useful test case to validate the proposed method and analyze its performance with different paradigms and algorithmic choices in Streaming OpInf. We present the problem setup, evaluation metrics, and results with discussions in Sections 4.1.1 to 4.1.3, respectively.

4.1.1. Problem Setup

The governing PDE is

$$\frac{\partial}{\partial t} x(\omega, t) = \mu \frac{\partial^2}{\partial \omega^2} x(\omega, t) - x(\omega, t) \frac{\partial}{\partial \omega} x(\omega, t), \quad (23)$$

where $x(\omega, t)$ represents the fluid velocity field, t denotes time, ω is the spatial coordinate, and $\mu > 0$ is the kinematic viscosity. This equation emerges from the Navier-Stokes equations through specific simplifications: restriction to one-dimensional flow and omission of pressure gradient effects. The first term represents viscous diffusion, while the second term captures nonlinear advective effects. Unlike the non-parametric formulation in eq. (1), we consider a parametric model reduction problem from the setup in [1] where the viscosity parameter μ varies across a prescribed range. After spatial discretization, the resulting full model takes the form:

$$\dot{\mathbf{x}}(t; \mu) = \mathbf{A}_1(\mu) \mathbf{x}(t; \mu) + \mathbf{A}_2(\mu) (\mathbf{x}(t; \mu) \otimes \mathbf{x}(t; \mu)) + \mathbf{B}(\mu) u(t),$$

where $\mathbf{x}(t; \mu) \in \mathbb{R}^n$ represents the state vector, $\mathbf{A}_1(\mu) \in \mathbb{R}^{n \times n}$ is the linear operator matrix, $\mathbf{A}_2(\mu) \in \mathbb{R}^{n \times n^2}$ is the quadratic operator matrix, and $\mathbf{B}(\mu) \in \mathbb{R}^{n \times 1}$ is the input operator matrix for a specific viscosity parameter μ .

We consider the spatial domain $\omega \in [0, 1]$ with Dirichlet boundary conditions controlled by the input: $x(0, t) = u(t)$ and $x(1, t) = -u(t)$. The initial condition is specified as $x(\omega, 0) = 0.1 \sin(2\pi\omega)$, and the simulation time extends from $t = 0$ to $t = 1.0$. The viscosity parameter is set to $\mu_i \in \{0.1, 0.2, \dots, 1.0\}$ with $i = 1, \dots, M$ and $M = 10$ total parameter values. Spatial discretization employs $n = 128$ grid points using second-order central differences for the diffusion term

¹Experiment code: <https://github.com/smallpondtom/StreamingOpInf>

and leap-frog scheme for the advection term. Time integration is performed using the semi-implicit Euler method with time step $\delta t = 1 \times 10^{-4}$, where the linear diffusion term is treated implicitly and the nonlinear advection and control terms are handled explicitly.

For training data generation, we sample 10 parameter values μ_i from the parameter space. At each parameter value, we generate 10 independent trajectories with control inputs $u(t)$ drawn uniformly from $[0, 1]$. Pooling the time-series data from these trajectories yields $K = 10,001$ snapshots per parameter value (including initial conditions). This results in a total training dataset of $10K = 100,010$ snapshots across all parameter values. For the iSVD phase, we compute the SVD for the entire parameter space comprising these $10K$ snapshots. We investigate reduced dimensions $r \in \{1, 2, \dots, 14\}$. To benchmark the Streaming OpInf method, we consider iSVD-LS and iSVD-RLS paradigms, where the time derivative data is approximated using first-order finite differences.

Training models are evaluated using a constant reference input $u(t) = 1.0$ for $t \in [0, 1]$. We learn one set of reduced operators per training parameter value μ_i . For new parameter values within the training range, we obtain the corresponding operators via element-wise B-spline interpolation (degree three) of the learned operator coefficients [106]. For generalization testing, we generate five new sets of reduced operators with five parameter values uniformly sampled within $[0.1, 1.0]$ and evaluate them on the same temporal grid with reference input $u(t) = 1.0$. We compute the SVD using both Baker's iSVD and SketchySVD methods for comparison, with the SVD components from SketchySVD used in the subsequent LS phase due to better performance in the iSVD evaluations shown in the subsequent sections. Note that in the LS phase, regularization is $\gamma = 1 \times 10^{-9}$ in both batch and streaming methods.

4.1.2. Evaluation Metrics

iSVD Method Assessment. We measure the alignment between POD bases computed from full SVD and iSVD methods using the subspace angle error metric:

$$\text{Subspace Angle Error} = \frac{1}{\sqrt{2}} \|\mathbf{V}_{\text{batch}} \mathbf{V}_{\text{batch}}^\top - \mathbf{V}_{\text{isvd}} \mathbf{V}_{\text{isvd}}^\top\|_F = \|(\mathbf{I} - \cos \theta)^{1/2}\|_F, \quad (24)$$

where $\mathbf{V}_{\text{batch}} \in \mathbb{R}^{n \times r}$ is the POD basis from full SVD, $\mathbf{V}_{\text{isvd}} \in \mathbb{R}^{n \times r}$ is the POD basis from iSVD, and $\cos \theta = \text{diag}(\sigma(\mathbf{V}_{\text{batch}}^\top \mathbf{V}_{\text{isvd}}))$ with $\sigma(\cdot)$ representing the singular values. Smaller values indicate better subspace alignment [107]. Additionally, we assess the approximation quality solely based on the POD basis using the relative projection error:

$$\text{Relative Projection Error} = \frac{\|\mathbf{X} - \mathbf{V}_r \mathbf{V}_r^\top \mathbf{X}\|_F}{\|\mathbf{X}\|_F}, \quad (25)$$

where \mathbf{X} is the snapshot matrix and \mathbf{V}_r is the rank- r POD basis.

Streaming Operator Learning Assessment. We monitor the operator convergence through the mean relative streaming operator error (MR-SOE) at stream k :

$$\text{MR-SOE}(k, r) = \frac{1}{M} \sum_{i=1}^M \frac{\|\mathbf{O}(\mu_i) - \mathbf{O}_k(\mu_i)\|_F}{dr \|\mathbf{O}(\mu_i)\|_F}, \quad (26)$$

where this quantity is averaged over all parameters, $\mathbf{O}_k(\mu_i)$ contains all reduced operators obtained via RLS at stream k with POD basis of rank- r , and the normalization factor dr accounts for the total number of operator elements. As discussed in Section 3.3, this metric provides insight into the convergence behavior of streaming operator estimates.

We further evaluate the streaming reconstruction accuracy using the mean relative streaming state error (MR-SSE) at stream k :

$$\text{MR-SSE}(k, r) = \frac{1}{M} \sum_{i=1}^M \frac{\|\mathbf{X}(\mu_i) - \mathbf{V}_r \tilde{\mathbf{X}}_k(\mu_i)\|_F}{\|\mathbf{X}(\mu_i)\|_F}, \quad (27)$$

where $\tilde{\mathbf{X}}_k(\mu_i)$ is the state trajectory simulated using the reduced model obtained at stream k for parameter μ_i . We track MR-SOE and MR-SSE at each data stream for different reduced dimensions r , reporting results for both RLS and iQRRLS algorithms. We additionally present the final reconstruction accuracy using the final relative state error (Final RSE) over different reduced dimensions r after processing all data streams, which is equivalent to $\text{MR-SSE}(K, r)$. We compute the final RSEs for both training and testing datasets, comparing streaming models against baselines: intrusive POD and standard OpInf with Tikhonov regularization.

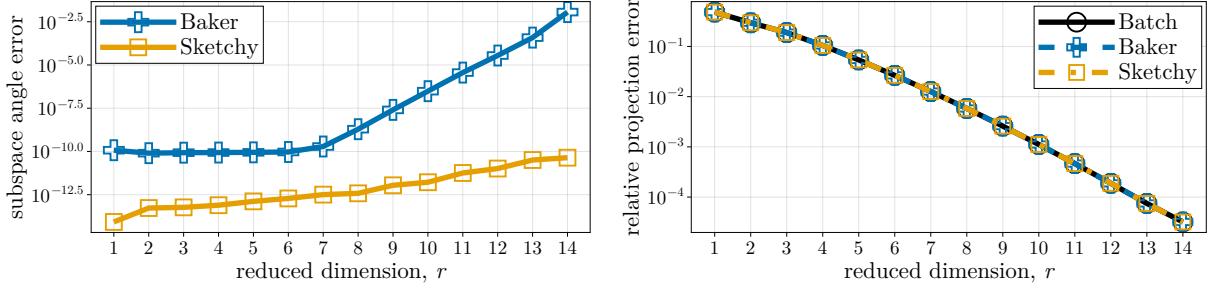


Figure 2: Burgers' Streaming SVD Assessment. **Left:** Subspace angles between POD bases computed from full SVD and iSVD methods. **Right:** Relative projection errors of the snapshot matrix onto POD bases for all SVD methods.

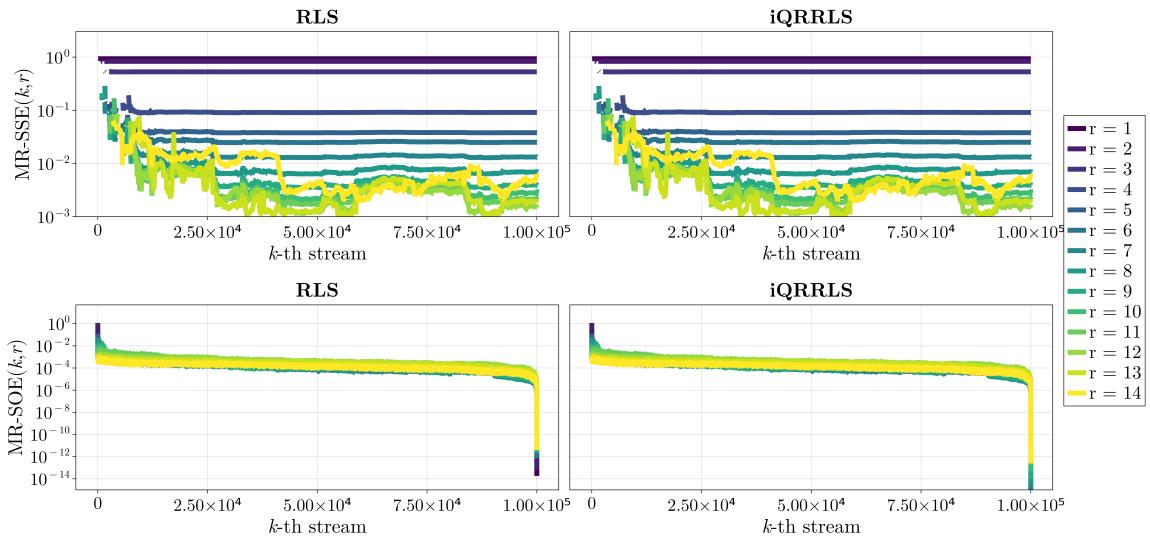


Figure 3: Burgers' RLS Assessment. **Top:** Relative state error averaged over all parameters at each stream. **Bottom:** Relative streaming operator error normalized by the total number of operator elements, averaged over all parameters at each stream. Gradient lines represent different reduced dimensions r .

4.1.3. Results & Discussion

Figure 2 compares iSVD methods against full SVD, showing subspace angle errors between the streaming SVD methods and the batch SVD (left) and relative projection errors (right). SketchySVD exhibits superior subspace alignment across all reduced dimensions r , particularly for higher-dimensional subspaces where smaller singular values are included. This aligns with theoretical predictions [97]: Baker's iSVD is more sensitive to spectral gap closure, while SketchySVD maintains lower errors through a tight error bound determined by a sufficiently large sketch size, as discussed in Section 2.2. The gradual increase in subspace angles reflects higher relative errors in smaller singular values. Moreover, both iSVD methods maintain projection errors comparable to batch SVD showing their reliability as alternatives for standard SVD.

Figure 3 illustrates the evolution of relative state errors (top) and streaming operator errors (bottom) throughout the streaming process. State errors decrease with fluctuations from incremental updates, ultimately plateauing for all r , confirming that RLS effectively refines the operator solution with each stream. Operator errors decrease sharply initially, plateau during the middle phase, then drop dramatically to near machine precision at the final stream when the update incorporates the full data. Higher r yields lower final state errors due to greater energy retention, while operator errors remain within the same order of magnitude across dimensions. Notably, state errors converge much earlier than operator errors reach machine precision, suggesting that approximate operator estimates can still yield accurate state reconstructions.

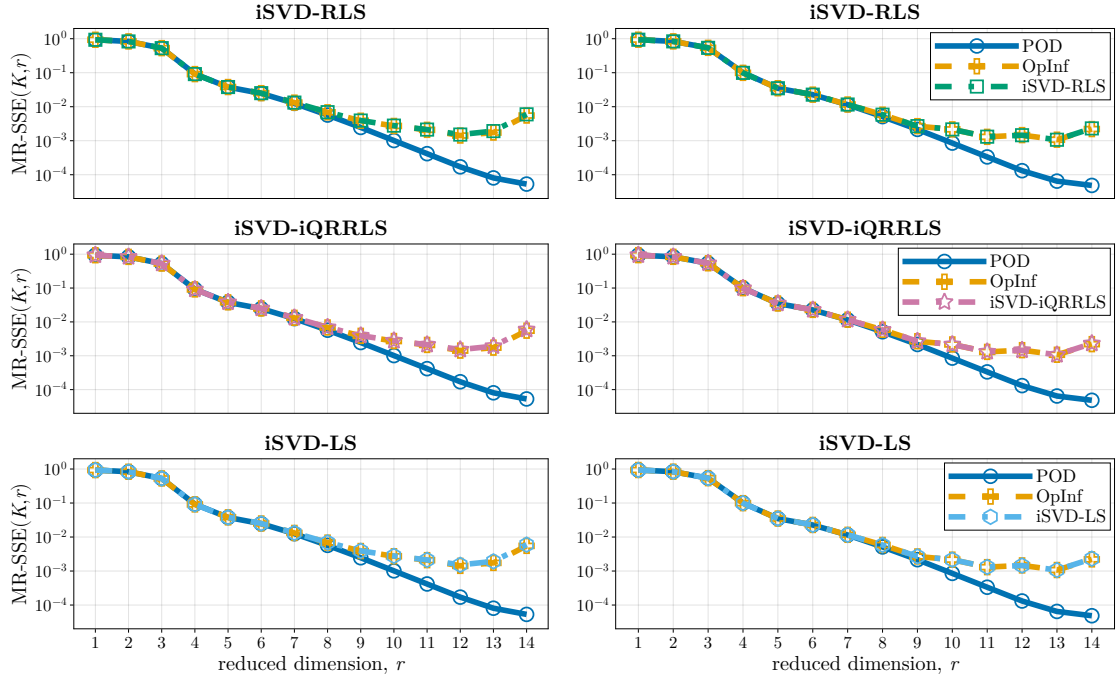


Figure 4: **Left Column:** Final relative state errors for training data across all reduced dimensions r for Burgers' equation. **Right Column:** Final relative state errors for testing data across all reduced dimensions r .

Figure 4 presents the final relative state errors for both training (left) and testing data (right) across all reduced dimensions r and Streaming OpInf paradigms. We observe that the final relative state errors for both training and testing data decrease monotonically with increasing reduced dimension r up to $r \approx 10$, beyond which closure errors—arising from unmodeled dynamics in the reduced space—cause the error to level out, whereas the intrusive POD method continues to decrease beyond this point [1]. Moreover, the testing results indicate successful generalization of the Streaming OpInf models within the trained parameter range. The slight error increase observed at $r = 13, 14$ for less important POD modes reflects numerical ill-conditioning in the LS problem caused by the abundance of steady-state data at the end of trajectories for higher viscosity parameters, consistent with observations in [1]. Nevertheless, as shown in Table 5, which shows memory costs and savings for all experiments, we see that Streaming OpInf reduces total memory usage by over 99% while obtaining comparable accuracy to the standard OpInf for this example.

These results validate that Streaming OpInf on a benchmark problem, achieving accuracy comparable to batch OpInf while providing substantial memory efficiency and scalability for streaming applications.

4.2. Kuramoto-Sivashinsky Equation

Next, we examine the Kuramoto-Sivashinsky Equation (KSE), a canonical example of spatiotemporal chaos originally developed to model flame propagation [108, 109]. Although this small-scale problem does not require data streaming, KSE's rich nonlinear dynamics make it a popular benchmark for model reduction [17, 110, 111] and a useful test case for evaluating Streaming OpInf on chaotic systems before applying it to larger-scale turbulent problems. We present the problem setup, evaluation metrics, and results with discussions in Sections 4.2.1 to 4.2.3, respectively.

4.2.1. Problem Setup

The governing partial differential equation is

$$\frac{\partial}{\partial t} x(\omega, t) + \frac{\partial^2}{\partial \omega^2} x(\omega, t) + \mu \frac{\partial^4}{\partial \omega^4} x(\omega, t) + x(\omega, t) \frac{\partial}{\partial \omega} x(\omega, t) = 0, \quad (28)$$

where $x(\omega, t)$ is the flame front position, ω is the spatial coordinate, and $\mu > 0$ is the kinematic viscosity. KSE incorporates temporal evolution, destabilizing second-order diffusion, stabilizing fourth-order hyperdiffusion, and nonlinear convection, with these competing effects producing complex spatiotemporal dynamics [112, 113].

For this investigation, we focus on a single parameter value $\mu = 1$ with no external control input. After spatial discretization, the resulting model takes the quadratic form:

$$\dot{\mathbf{x}}(t) = \mathbf{A}_1 \mathbf{x}(t) + \mathbf{A}_2 (\mathbf{x}(t) \otimes \mathbf{x}(t)),$$

where $\mathbf{x}(t) \in \mathbb{R}^n$ is the state vector, $\mathbf{A}_1 \in \mathbb{R}^{n \times n}$ and $\mathbf{A}_2 \in \mathbb{R}^{n \times n^2}$ are as defined in (1).

Following the computational setup from [17], we define the spatial domain as $\omega \in [0, L]$ with $L = 22$ and periodic boundary conditions. The domain length $L = 22$ is chosen to ensure the system exhibits chaotic dynamics while maintaining computational tractability [114]. The initial condition is specified as $x(\omega, 0) = a \cos(2\pi\omega/L) + b \cos(4\pi\omega/L)$, where $a \in \{0.2, 0.7, 1.2\}$ and $b \in \{0.1, 0.5, 0.9\}$ are amplitude parameters that control the initial perturbation strength.

The spatial discretization employs $n = 512$ uniformly distributed grid points, providing adequate resolution to capture the fine-scale structures characteristic of the KSE dynamics. Time integration is performed using a semi-implicit scheme that combines the second-order Crank-Nicolson method for the linear terms (second and fourth-order derivatives) with the second-order Adams-Basforth method for the nonlinear convection term. This hybrid approach ensures numerical stability while maintaining temporal accuracy. The time step is set to $\delta t = 1 \times 10^{-3}$, and simulations extend from $t = 0$ to $t = 300$, capturing both transient and fully developed chaotic regimes.

The training dataset comprises 9 trajectories generated from all combinations of the amplitude parameters a and b . Time derivative data is approximated using first-order finite differences applied to the solution snapshots. To reduce computational burden while preserving essential dynamics, both snapshot and time derivative data are downsampled by retaining every 100th time step, resulting in $K = 3,000$ snapshots per trajectory and a total of $9K = 27,000$ snapshots across all trajectories. For the iSVD phase, we compute the SVD for the entire dataset of $9K$ snapshots. We investigate reduced dimensions $r \in \{9, 12, 15, 18, 21, 24\}$.

For generalization assessment, testing data is generated using 50 additional combinations of amplitude parameters (a, b) drawn uniformly from the continuous ranges $a \in [0.2, 1.2]$ and $b \in [0.1, 0.9]$. These testing models are evaluated on the same temporal grid as the training data. We compute the SVD using both Baker's iSVD and SketchySVD methods for comparison, with the SVD components from Baker's iSVD deliberately chosen for the subsequent LS phase to explore the impact of different iSVD methods on final model performance.

In this example, we employ both the standard RLS and iQRRLS algorithms to solve the LS problem at each data stream. The Tikhonov regularization parameter is set to $\Gamma = \gamma \mathbf{I}_d$ with $\gamma = 1 \times 10^{-9}$ for both streaming and batch Tikhonov-regularized OplInf methods, providing minimal regularization while ensuring numerical stability.

Since the provided data includes both downsampled snapshot data and time-derivative data, using finite difference to approximate the time derivative will introduce significant errors in the operator inference process. Hence, this experiment specifically applies the iSVD-Projection-RLS paradigm in Section 3.2, where both downsampled snapshot data and time derivative data are directly projected onto the POD basis to form the reduced data.

4.2.2. Evaluation Metrics

For iSVD assessment, we measure subspace alignment using subspace angles and approximation quality using relative projection errors, as in Section 4.1.2. For streaming operator learning, we track only the MR-SOE at each stream with $M = 1$. Unlike the Burgers' equation case, we omit state error metrics because KSE's chaotic dynamics cause exponentially diverging trajectories from small perturbations, making point-wise error metrics less meaningful. Hence, it is crucial that we capture the statistical properties and attractor geometry of the chaotic system using Quantities of Interest (QoIs) that show dynamical invariants, i.e., invariants to initial conditions and individual trajectories.

The first QoI we compute is the leading 10 Lyapunov exponents (LEs) $(\lambda_1, \lambda_2, \dots, \lambda_{10})$, which quantify the average exponential rate of trajectory divergence or convergence in phase space [115], with positive LEs indicating chaotic directions and negative LEs representing stable directions. LEs are computed using the algorithm from [116, 117], averaging over all trajectories for training and testing datasets and comparing against the full model and batch methods.

The second QoI is the Kaplan-Yorke dimension (KY-dimension) computed from the Lyapunov spectrum, which estimates the fractal dimension of the chaotic attractor [118, 119]: $D_{KY} = j + \frac{\sum_{i=1}^j \lambda_i}{|\lambda_{j+1}|}$, where j is the largest integer such that $\sum_{i=1}^j \lambda_i \geq 0$. We validate our computed values against reference values in [120]. Moreover, for qualitative

assessment, we present spatiotemporal flow field predictions for representative trajectories from both training and testing datasets.

4.2.3. Results & Discussion

Figure 5 presents the performance comparison between Baker’s iSVD and SketchySVD methods. The left panel shows subspace angles relative to the full SVD basis, while the right panel displays relative projection errors. Both methods exhibit precise subspace alignment for reduced dimensions up to $r = 12$, with Baker’s iSVD showing substantially larger alignment errors for higher dimensions. This behavior agrees with the results in the Burgers’ equation example. The projection error comparison demonstrates that both iSVD methods maintain approximation quality comparable to full SVD across all investigated dimensions. As observed in the Burgers’ equation experiment, SketchySVD demonstrates superior accuracy in subspace alignment. However, we deliberately employ Baker’s iSVD components in the subsequent LS phase to investigate the robustness of the streaming approach to suboptimal basis selection.

Figure 6 illustrates the evolution of relative streaming operator errors, revealing distinct behaviors between RLS and iQRRLS algorithms. The iQRRLS algorithm exhibits the characteristic sharp error decrease near final streams, similar to the Burgers’ experiment, while standard RLS displays acute error spikes throughout streaming without dramatic final improvement. This difference stems from numerical conditioning, in which iQRRLS maintains superior conditioning through QR factorization-based updates, providing robustness even as \mathbf{P}_k becomes ill-conditioned, while standard RLS becomes susceptible to numerical instabilities as more data streams are processed. Overall, iQRRLS demonstrates more near machine-precision convergence to the batch OpInf solution across all reduced dimensions.

Figure 7 presents a qualitative comparison of spatiotemporal flow field predictions for representative trajectories from training and testing datasets using $r = 24$. The top row displays the characteristic spatiotemporal evolution patterns, while the bottom row shows absolute errors relative to the full model. All learning approaches successfully capture the primary flow features and spatiotemporal patterns of the full model, with error magnitudes comparable to intrusive POD, indicating similar approximation quality. The absolute errors can exceed flow field magnitudes in

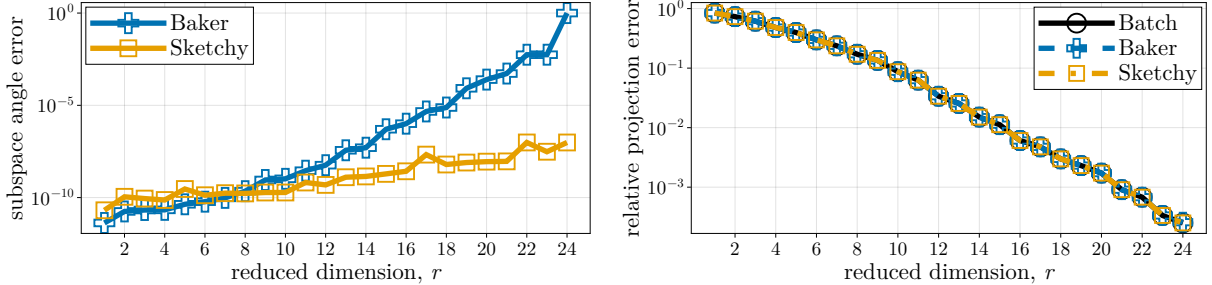


Figure 5: KSE Streaming SVD Assessment. **Left:** Subspace angles between POD bases computed from full SVD and iSVD methods. **Right:** Relative projection errors of the snapshot matrix onto POD bases computed from iSVD methods.

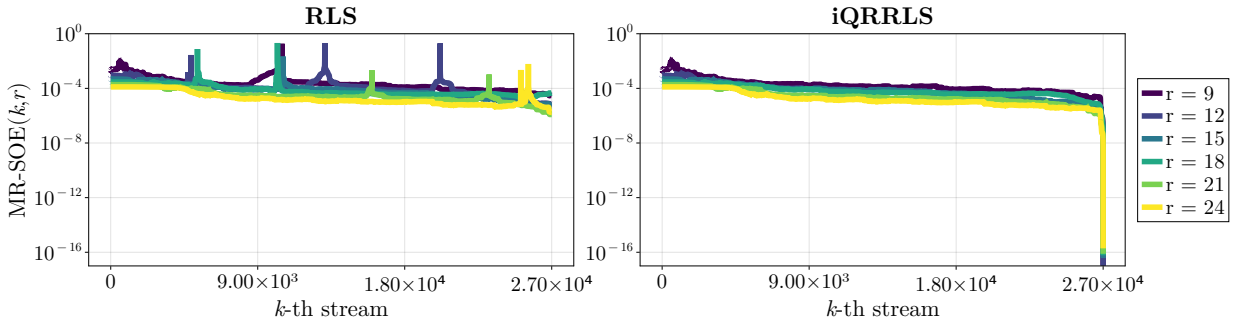


Figure 6: KSE RLS Assessment. Relative streaming operator error normalized by the total number of operator elements, averaged over all trajectories at each stream. Gradient lines represent different reduced dimensions r .

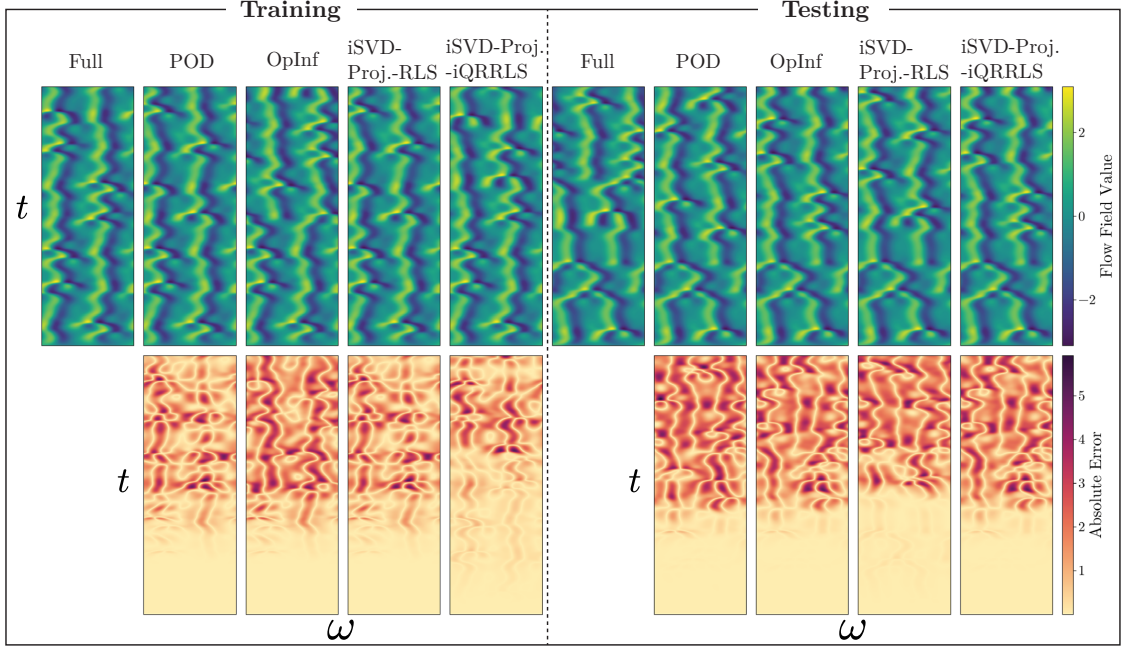


Figure 7: Comparison of KSE flow field predictions for training (left box) and testing (right box) data using full model and reduced models with $r = 24$. **Row 1:** Predictions for training and testing trajectories with initial condition parameters $(a, b) = (0.2, 0.5)$ and $(0.6869, 0.4186)$, respectively. **Row 2:** Absolute errors between full model and reduced models. Time evolves from bottom to top. “iSVD-Proj.-RLS” and “iSVD-Proj.-iQRRLS” indicate iSVD-Projection paradigms.

certain regions, which is characteristic of chaotic systems where trajectories exponentially diverge and lead to phase-shifts. Moreover, error patterns show larger magnitudes in the latter portion of the domain (top half of error plots) compared to the initial transient region, reflecting the challenge of representing fully developed chaotic dynamics where small discrepancies amplify over time. Nevertheless, the bounded errors without unphysical growth confirm that the reduced models remain dynamically consistent.

Figure 8 assesses the learned models’ ability to predict dynamical invariants. The first two columns show the Lyapunov spectrum (first 10 largest exponents) for $r = 24$ compared to reference values [120]. All reduced models successfully capture both positive Lyapunov exponents and negative exponents, which is crucial for maintaining the correct balance between expansion and contraction in phase space. The Kaplan-Yorke dimension analysis (third column) reveals close agreement with reference values [120] for specific dimensions ($r = 9, 21, 24$), with larger deviations for intermediate values ($r = 12, 15, 18$). This non-monotonic behavior reflects the metric’s sensitive dependence on precise Lyapunov exponent values, where small errors in individual exponents propagate when $\sum_{i=1}^j \lambda_i$ approaches zero. Both RLS and iQRRLS variants achieve dynamical invariants comparable to batch methods.

In summary, our results demonstrate that Streaming OpInf preserves essential dynamical characteristics of chaotic systems while providing over 99% memory savings compared to batch methods as shown in Table 5. The preservation of Lyapunov exponents and accurate approximation of fractal dimensions confirm that the streaming approach captures the fundamental geometric and dynamical properties of the underlying attractor, making it suitable for applications requiring long-term statistical accuracy.

4.3. Turbulent Channel Flow

The final numerical experiment examines three-dimensional turbulent channel flow at high Reynolds number, a problem whose large-scale data requirements exceed available memory and necessitate streaming methods. This canonical wall-bounded turbulent flow is pressure-driven between parallel walls and exhibits complex three-dimensional velocity structures that have been extensively studied to understand turbulence physics near boundaries. We perform simulations of a symmetric half-channel flow using a wall-modeled large eddy simulations (LES) formulation described in Section 4.3.1, with evaluation metrics and results presented in Sections 4.3.2 and 4.3.3, respectively.

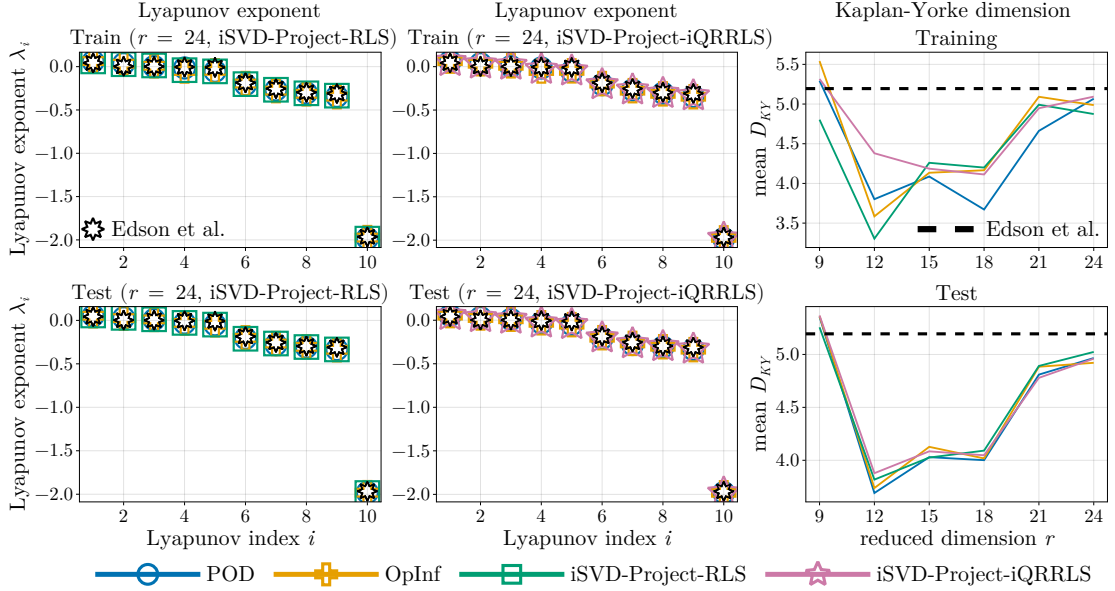


Figure 8: KSE QoI Assessment. **Columns 1 & 2:** First 10 largest Lyapunov exponents for training and testing data with $r = 24$. **Column 3:** Kaplan-Yorke dimensions for training and testing data across all reduced dimensions. Streaming-OpInf models are “iSVD-Project-RLS” and “iSVD-Project-iQRRRLS”. Black markers and lines represent reference LE values and KY-dimensions from [120].

4.3.1. Problem Setup

We use AMR-Wind, a parallel, block-structured adaptive-mesh incompressible flow solver, to perform wall-modeled LES of the channel flow [121, 122]. AMR-Wind solves the LES formulation of the incompressible Navier-Stokes (NS) equations. With (\cdot) denoting the spatial filtering operator, the governing equations in Cartesian coordinates using Einstein notation are

$$\frac{\partial \tilde{u}_j}{\partial \omega_j} = 0, \quad (29)$$

$$\frac{\partial \tilde{u}_i}{\partial t} + \frac{\partial \tilde{u}_i \tilde{u}_j}{\partial \omega_j} = -\frac{1}{\rho} \frac{\partial \tilde{p}}{\partial \omega_i} - \frac{\partial \tau_{ij}}{\partial \omega_j} + \nu \frac{\partial^2 \tilde{u}_i}{\partial \omega_j \partial \omega_i} + F_i, \quad (30)$$

where ω_i denotes the coordinate in direction $i = \{1, 2, 3\}$, \tilde{u}_i is the filtered velocity, \tilde{p} is the pressure, ν is the molecular viscosity, ρ is the density, and τ_{ij} are the subgrid stress terms representing interactions with unresolved scales, defined as $\tau_{ij} = \tilde{u}_i \tilde{u}_j - \tilde{u}_i \tilde{u}_j$. The forcing term F_i drives the flow, and each direction i corresponds to the streamwise, spanwise, and wall-normal directions, respectively.

The Smagorinsky eddy viscosity model is used to model τ_{ij} , where the dissipation is calculated as:

$$\tau_{ij} = -2\nu_t \tilde{S}_{ij}, \quad \nu_t = C_s^2 (2\tilde{S}_{ij} \tilde{S}_{ij})^{\frac{1}{2}} \Omega^2, \quad \tilde{S}_{ij} = \frac{1}{2} \left(\frac{\partial \tilde{u}_i}{\partial \omega_j} + \frac{\partial \tilde{u}_j}{\partial \omega_i} \right),$$

where \tilde{S}_{ij} is the resolved strain rate tensor, C_s is the Smagorinsky constant set to 0.1, and Ω is the filter width defined by $\Omega = \sqrt[3]{\delta\omega_1 \times \delta\omega_2 \times \delta\omega_3}$ with $\delta\omega_i$ denoting the grid spacing in direction i .

AMR-Wind employs discretization schemes that are second-order accurate in both space and time. The spatial discretization is a second-order finite-volume method. Velocity, scalar quantities, and pressure gradients are located at cell centers, whereas pressure is located at nodes. In addition to spatial staggering, the temporal discretization employs staggering similar to a Crank-Nicolson formulation.

The boundary conditions for the half-channel simulation are periodic in the streamwise and spanwise directions. A log-law-based wall model is applied at the bottom boundary, and centerline symmetry conditions are imposed at the top boundary. The flow is driven by a constant streamwise pressure gradient.

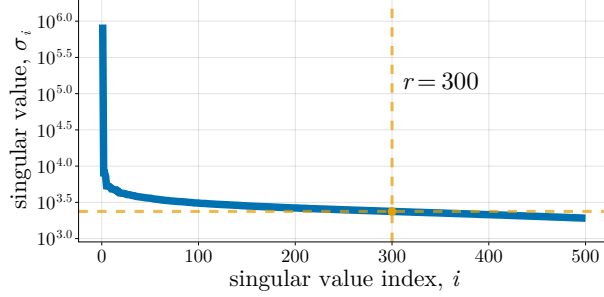


Figure 9: Spectral decay of the turbulent channel flow example for 500 singular values.

Denoting the full state as $\mathbf{x} = [\tilde{u}_1, \tilde{u}_2, \tilde{u}_3, p]^\top$, and recognizing that the NS equations are governed by quadratic nonlinearity, we assume the spatially discretized form of the governing equations is quadratic with a constant term arising from the forcing and from the mean-centering and normalization described in Section 3.4. The ODE model thus takes the form:

$$\dot{\mathbf{x}}(t) = \mathbf{A}_1 \mathbf{x}(t) + \mathbf{A}_2(\mathbf{x}(t) \otimes \mathbf{x}(t)) + \mathbf{c},$$

where the full state vector is $\mathbf{x} \in \mathbb{R}^n$.

The data are generated at a high friction Reynolds number $Re_\tau = 5,200$ and discretized on a finite-volume grid of $384 \times 192 \times 32$ cells in the streamwise, spanwise, and wall-normal directions, respectively, yielding a full state dimension of $n = 384 \times 192 \times 32 \times 4 = 9,437,184$. We collect 10,000 consecutive snapshots after the simulation reaches a statistically stationary state.

Normalized by L , the half-channel width, the domain size is $[12L, 6L, 1L]$, the molecular viscosity is $\nu = 8 \times 10^{-6}$, and the forcing term is a constant streamwise pressure gradient given by $F_{\omega_1} = \frac{d\bar{p}}{d\omega_1} = \bar{u}_\tau^{-2}$, where $\bar{u}_\tau = 0.0415$ is the mean friction velocity. The time stepping is adjusted to maintain a constant CFL number of 0.95 throughout the simulation, corresponding to a time step of $\delta t \approx 0.023$. The total simulation time of 10,000 time steps corresponds to approximately 10 units of L/u_τ , capturing sufficient dynamics of this highly chaotic system to demonstrate our reduced operator learning approach.

We partition the 10,000 snapshots by taking the first 8,000 as training snapshots and the remaining 2,000 as testing snapshots. The data are preprocessed via mean-centering followed by normalization to the range $[-1, 1]$, where each grid point is normalized individually using its temporal mean, minimum, and maximum values.

Figure 9 shows the spectral decay of the training data up to 500 modes, revealing the significant challenges posed by this turbulent flow. The slow spectral decay, where singular values remain on the order of 10^3 for many modes (presumably even beyond 500 modes), indicates that a large number of modes are required to capture the flow dynamics accurately. To address this challenge, we compute the SVD components using the SketchySVD method, which, despite slightly higher memory requirements, provides superior accuracy in low-dimensional approximation compared to Baker's method as demonstrated in the previous experiments. We construct a POD basis of dimension 500 to improve accuracy by reducing errors from larger truncated singular values, as discussed in Section 2.2, and investigate reduced operators of dimension $r = 300$. Time derivatives are approximated using fourth-order central differences in the interior with fourth-order forward and backward differences at the boundaries.

We will learn the reduced operators using iSVD-LS. Finally, 4th-order Runge-Kutta scheme is used to integrate the learned reduced model in time. Given the problem's complexity, Tikhonov regularization parameters for the LS are carefully selected via grid search over 25 log-equidistant points in $\gamma_1 \in [10^6, 10^{12}]$ and 20 log-equidistant points in $\gamma_2 \in [10^{12}, 10^{16}]$. The optimal parameters are found to be $(\gamma_1, \gamma_2) = (1.7783 \times 10^7, 4.2813 \times 10^{12})$. These high regularization values align with our discussion of mitigating operator errors in Section 3.3.1.

4.3.2. Evaluation Metrics

The channel flow is a highly turbulent dynamical system with a large number of positive Lyapunov exponents. Hence, similar to the KSE example, point-wise error metrics are not very meaningful for this problem. Thus, we focus on an assessment of the flow field predictions, where we compare two-dimensional slices of the flow field at

specific time instances, and two important QoIs that are commonly used in the fluid mechanics community to assess the accuracy of turbulent channel flow simulations.

The first QoI is the friction velocity u_τ , which is an important scaling parameter for wall-bounded turbulent flows [123, 124]. In our problem, the friction velocity oscillates around the target mean \bar{u}_τ used in the forcing term, and thus, we report the target mean values and visualize the friction velocity normalized by the target mean, i.e., u_τ/\bar{u}_τ .

The second QoI is the wall-normal profile of the streamwise velocity u_1 , which represents the spatial characteristics of the flow, exhibiting a low-law profile for the mean velocity given by [125]:

$$\frac{u_1}{u_\tau} = \frac{1}{\kappa} \log \left(\frac{u_\tau \omega_3}{\nu} \right) + B, \quad (31)$$

where κ is the von Karman constant, and B is an intercept constant. The two QoIs are computed for both the training and testing data and compared with the results from the original data.

4.3.3. Results & Discussion

Table 4: Target mean of friction velocity \bar{u}_τ compared with the mean values from training and testing data calculated by computing the friction velocities then averaging them over time. Errors are relative to the reference value of $\bar{u}_\tau = 0.0415$.

	Training \bar{u}_τ (Rel. Error %)	Testing \bar{u}_τ (Rel. Error %)
Original Data	0.04137 (0.3049%)	0.04119 (0.7364%)
Streaming OpInf	0.04126 (0.5611%)	0.04130 (0.4857%)

Assessment of the Flow Field Predictions. Figure 10 present two-dimensional slices of the three-dimensional turbulent channel flow field at 3 or 2 temporal instances during training and testing, respectively. The visualizations focus on the streamwise velocity component \tilde{u}_1 , which exhibits the most energetic turbulent structures. The first row displays the original high-fidelity data, the second row shows predictions from Streaming OpInf with reduced dimension $r = 300$, and the third row presents the POD projection as a benchmark for the best achievable accuracy given the same reduced dimensionality. The fourth and fifth rows visualize the absolute errors between the original data and the Streaming OpInf predictions and POD projections, respectively.

During the training phase in Figure 10, Streaming OpInf successfully captures the complex turbulent structures characteristic of wall-bounded flows, including the elongated streaks and smaller-scale vortical structures similar to the original data across all temporal instances, demonstrating the method’s ability to learn the underlying dynamics from streaming data. The POD projection results in the third and fifth row provide a visual reference for the inherent approximation error introduced by dimensionality reduction alone, independent of the operator learning process. Compared to the projection errors, the error distribution of Streaming OpInf (fourth row) remains at a comparable magnitude and is spatially distributed throughout the domain. This indicates that the learned reduced operators accurately capture the system dynamics without introducing significant additional modeling error beyond the truncation error from dimensionality reduction.

The testing phase results in Figure 10 demonstrate the model’s predictive capability on unseen data. The Streaming OpInf predictions maintain their fidelity to the original flow structures throughout the testing period, successfully reproducing the characteristic turbulent patterns. Further, the Streaming OpInf predictions present the spatial patterns more clearly than the POD projections. The error magnitudes and distributions remain consistent with those observed during training, indicating that the learned reduced model generalizes well without overfitting to the training data. This is particularly significant given the chaotic nature of turbulent flows, where small perturbations can lead to trajectory divergence. The sustained accuracy across 2,000 testing snapshots (approximately 2.5 time units of L/u_τ) demonstrates the robustness of the learned reduced operators.

Quantitative Assessment via Quantities of Interest. Figure 11 displays the friction velocity u_τ evolution over time. The top panel shows both the original and predicted friction velocities normalized by the target mean friction velocity

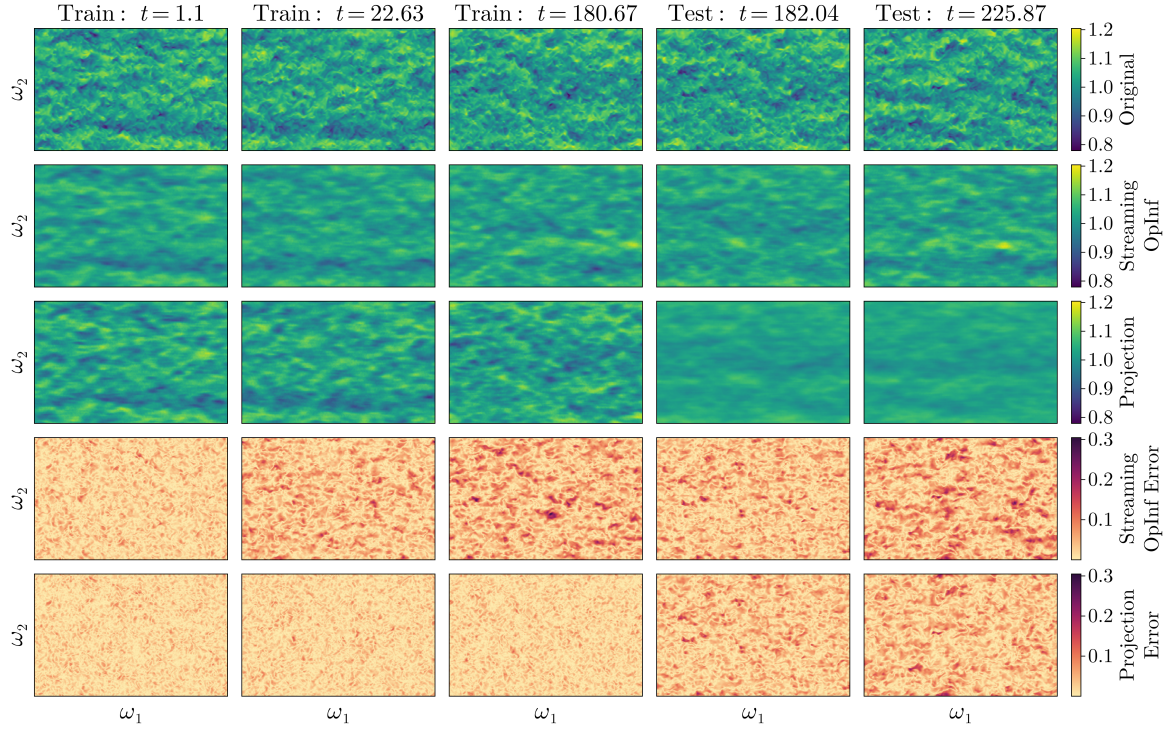


Figure 10: Comparison of 2D slices of the turbulent channel flow field predictions for training and testing data of the **streamwise velocity** component. First row is the original data, the second row is the prediction from Streaming-OpInf with $r = 300$, the third row is the projection result from POD with $r = 300$, and the last two rows is the absolute error between the original data and the prediction from Streaming-OpInf and POD, respectively. Time evolves from left to right.

\bar{u}_τ computed by averaging the calculated friction velocities over time. Streaming OpInf show similar temporal fluctuations compared to the original data for both training and testing phases, capturing the characteristic variations arising from the passage of turbulent structures near the wall. The bottom panel presents the relative errors on a logarithmic scale, revealing errors consistently below 10^{-2} for the majority of snapshots, with occasional spikes reaching 10^{-5} that correspond to particularly strong instantaneous overlaps between the predicted and true friction velocities.

Figure 12 presents the wall-normal profile of the time-averaged streamwise velocity component. The logarithmic scale on the wall-normal coordinate axis emphasizes the near-wall region where velocity gradients are steepest [123]. For both training and testing data, Streaming OpInf predictions closely match the original data across the entire wall-normal extent, accurately capturing both the viscous sublayer near the wall and the turbulent/logarithmic layer in the outer region while adhering to the log-law (31) [126, 127]. The relative errors, shown in the bottom panels, remain below 10^{-3} for training and 10^{-2} for testing throughout most of the domain, with slightly elevated errors in the near-wall region where the flow physics are most complex. The consistency between training and testing errors confirms the model’s ability to preserve statistical properties of the turbulent flow.

Table 4 quantifies the time-averaged friction velocities for both training and testing data, comparing them against the target value $\bar{u}_\tau = 0.0415$ specified in the simulation setup. The Streaming OpInf predictions yield mean friction velocities of 0.04126 and 0.04130 for training and testing data, respectively, closely matching both the original data statistics (0.04137 and 0.04119) and the target value. The relative errors of approximately 0.5% demonstrate that Streaming OpInf preserves the global flow statistics with high fidelity, an essential requirement for reduced models intended to replace high-fidelity simulations in many-query scenarios.

Discussion. The results show that Streaming OpInf successfully learns accurate reduced models for a highly challenging large-scale turbulent flow problem. Starting from over 9 million degrees of freedom, the method achieves a state dimension reduction exceeding 31,000x while maintaining high predictive accuracy and enabling significantly

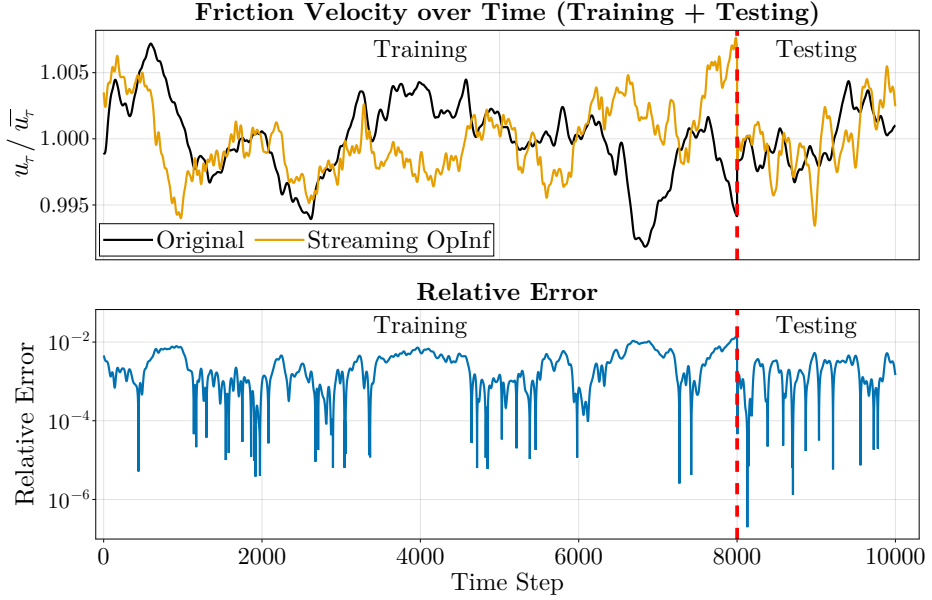


Figure 11: (QoI 1) Friction velocity u_r for training and testing data.

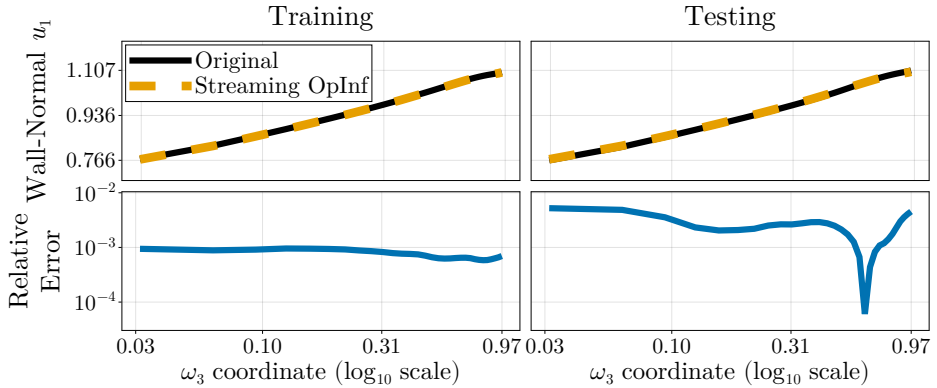


Figure 12: (QoI 2) Wall normal profile of the streamwise velocity component for training and testing data.

faster state predictions. The streaming approach processes this large-scale dataset sequentially without requiring simultaneous access to all 8,000 snapshots, directly addressing the storage bottleneck in traditional batch methods.

For turbulent channel flow, Streaming OpInf realizes 76% memory reduction for the SVD process and 68% total reduction compared to batch OpInf (Table 5). These substantial savings, combined with sequential data processing, establish the framework's suitability for real-time applications with continuous data arrival and limited storage.

Several algorithmic choices contribute to success in this challenging application: (i) selecting $r = 300$ captures dominant turbulent structures with sufficient energy retention, (ii) careful calibration of Tikhonov regularization (γ_1, γ_2) through systematic grid search prevents overfitting while promoting stable operator learning despite chaotic dynamics, and (iii) employing SketchySVD achieves favorable trade-offs between computational efficiency and approximation accuracy for massive data matrices.

Finally, the comparable performance between training and testing phases demonstrates that learned operators capture essential physics governing turbulent channel flow for long-term accuracy rather than memorizing training patterns. The sustained fidelity in both instantaneous flow fields and time-averaged statistics demonstrates that Streaming OpInf preserves dynamical and statistical properties essential for reliable turbulence modeling.

Table 5: Memory cost comparison between batch and streaming approaches across all three experiments.

(a) Memory costs based on Tables 1 to 3				
Experiments	Batch SVD	Streaming SVD	Batch LS	Streaming OpInf LS
Burgers'	1.28e+07	8.32e+03	1.21e+06	1.44e+04
KSE	1.38e+07	1.23e+04	1.08e+06	1.05e+05
Channel flow	1.96e+10	3.80e+09	2.43e+09	2.43e+09

(b) Memory cost reduction percentages			
Experiments	SVD Reduction	LS Reduction	Total Reduction
Burgers'	99.94%	98.81%	99.84%
KSE	99.91%	90.25%	99.21%
Channel flow	76.36%	0.00%	68.11%

5. Conclusion

In this work, we have developed a novel reduced operator learning approach that reformulates the traditional OpInf framework to a data-streaming context. By integrating iSVD with RLS methods, our method efficiently constructs the reduced operators by only relying on the SVD components and the current data sample, thus significantly reducing memory requirements and enabling the handling of large-scale datasets as well as online operator learning scenarios, which lays the groundwork for real-time applications.

We have explored various algorithmic choices within the Streaming OpInf framework, including different iSVD techniques (Baker’s method and SketchySVD) and operator learning strategies (a new reformulation of the batch LS and RLS methods). We have also presented practical strategies for choosing different algorithmic variations of the framework based on data availability and computational resources.

Through comprehensive numerical experiments on benchmark problems such as the one-dimensional viscous Burgers’ equation, the Kuramoto-Sivashinsky equation, and a large-scale turbulent channel flow simulation, we have demonstrated accuracy on par with traditional batch OpInf methods while achieving over 99% reductions in memory usage. The experiments also highlighted the importance of practical considerations such as data standardization and regularization in enhancing model performance and stability.

While the results are highly encouraging, some limitations warrant mention. Given the advection-dominant nature of the turbulent channel flow, $r = 300$ may still be insufficient to fully resolve all relevant scales, particularly in the near-wall region where velocity gradients are steepest. This is reflected in the friction velocity at later time instances where the trend deviates larger from the original data and the opaqueness compared to the original data in the flow field predictions of Figure 10. Future work could explore streaming formulations of more advanced reduced modeling methods, such as those utilizing nonlinear manifold approaches as demonstrated in [4, 6], which could potentially capture the complex flow physics with even lower dimensions. Additionally, extending the framework to accommodate more complex dynamical systems, exploring the combination of parallelization and streaming, and integrating uncertainty quantification techniques [13, 14] to further enhance the robustness of the learned models.

Overall, Streaming OpInf represents a significant advancement in the field of operator learning, providing a scalable, efficient solution for large-scale data scenarios and establishing foundations for rapid real-time predictions.

CRediT authorship contribution statement

Tomoki Koike: Writing - review & editing, Writing - original draft, Visualization, Validation, Software, Methodology, Investigation, Formal analysis, Data curation, Conceptualization; Prakash Mohan: Writing – review & editing, Supervision, Resources, Data curation; Marc T. Henry de Frahan: Writing - review & editing, Supervision, Resources, Data curation; Julie Bessac: Supervision, Funding Acquisition, Project administration; Elizabeth Qian: Conceptualization, Writing - review & editing, Supervision, Funding Acquisition, Project administration.

Data Availability

Data and experiment code are available at <https://github.com/smallpondtom/StreamingOpInf> for reproducibility. The main implementations for Streaming OpInf are available at <https://github.com/smallpondtom/LiftAndLearn.jl>.

Declaration of competing interest

The authors declare that they have no known competing financial interests or personal relationships that could have appeared to influence the work reported in this paper.

Acknowledgement

The authors were supported by the Department of Energy Office of Science Advanced Scientific Computing Research, DOE Award DE-SC0024721. This work was authored in part by NLR for the U.S. Department of Energy (DOE), operated under Contract No. DE-AC36-08GO28308. The views expressed in the article do not necessarily represent the views of the DOE or the U.S. Government. The U.S. Government retains and the publisher, by accepting the article for publication, acknowledges that the U.S. Government retains a nonexclusive, paid-up, irrevocable, worldwide license to publish or reproduce the published form of this work, or allow others to do so, for U.S. Government purposes. A portion of the research was performed using computational resources sponsored by the Department of Energy and located at the National Laboratory of the Rockies.

A. Streaming SVD Algorithms

Algorithm 1 Baker's iSVD Algorithm

Require: truncation dimension r , total number of data vectors K

```

1: Receive initial data vector  $\mathbf{x}_1$  and initialize:  $\mathbf{V}_{r_k} \Sigma_{r_k} \leftarrow \text{qr}(\mathbf{x}_1)$ ,  $\mathbf{W}_{r_k} \leftarrow 1$ ,  $r_k \leftarrow 1$ 
2: for  $k = 2$  to  $K$  do
3:   Receive new data vector:  $\mathbf{x}_k$ 
4:   Compute projection and residual:  $\mathbf{q} \leftarrow \mathbf{V}_{r_k}^\top \mathbf{x}_k$ ,  $\mathbf{x}_\perp \leftarrow \mathbf{x}_k - \mathbf{V}_{r_k} \mathbf{q}$ 
5:   Second orthogonalization:  $\mathbf{q}_2 \leftarrow \mathbf{V}_{r_k}^\top \mathbf{x}_\perp$ ,  $\mathbf{x}_\perp \leftarrow \mathbf{x}_\perp - \mathbf{V}_{r_k} \mathbf{q}_2$ ,  $\mathbf{q} \leftarrow \mathbf{q} + \mathbf{q}_2$ 
6:   QR decomposition of residual:  $\mathbf{x}_\perp p \leftarrow \text{qr}(\mathbf{x}_\perp)$ 
7:   Form augmented matrices:

$$\hat{\mathbf{V}} \leftarrow \begin{bmatrix} \mathbf{V}_{r_k} & \mathbf{x}_\perp \end{bmatrix}, \quad \mathbf{J} \leftarrow \begin{bmatrix} \Sigma_{r_k} & \mathbf{q} \\ \mathbf{0}_{1 \times r_k} & p \end{bmatrix}, \quad \hat{\mathbf{W}} \leftarrow \begin{bmatrix} \mathbf{W}_{r_k} & \mathbf{0}_{k \times 1} \\ \mathbf{0}_{1 \times r_k} & 1 \end{bmatrix}, \quad r_k \leftarrow r_k + 1$$

8:   Compute SVD:  $\mathbf{V}_J \Sigma_J \mathbf{W}_J^\top \leftarrow \text{svd}(\mathbf{J})$ 
9:   Update matrices:  $\mathbf{V}_{r_k} \leftarrow \hat{\mathbf{V}} \mathbf{V}_J$ ,  $\Sigma_{r_k} \leftarrow \Sigma_J$ ,  $\mathbf{W}_{r_k} \leftarrow \hat{\mathbf{W}} \mathbf{W}_J$ 
10:  if  $r_k > r$  then
11:    Truncate:  $\mathbf{V}_{r_k} \leftarrow \mathbf{V}_{r_k}(:, 1:r)$ ,  $\Sigma_{r_k} \leftarrow \Sigma_{r_k}(1:r, 1:r)$ ,  $\mathbf{W}_{r_k} \leftarrow \mathbf{W}_{r_k}(:, 1:r)$ ,  $r_k \leftarrow r$ 
12:  end if
13: end for
14: Return:  $\mathbf{V}_r$ ,  $\Sigma_r$ ,  $\mathbf{W}_r$ 

```

Algorithm 2 SketchySVD Algorithm

Require: truncation dimension r , total number of data vectors K , sketch sizes q and s

- 1: Initialize reduction maps: $\Upsilon \in \mathbb{R}^{q \times n}$, $\Omega \in \mathbb{R}^{q \times K}$, $\Xi \in \mathbb{R}^{s \times n}$, $\Psi \in \mathbb{R}^{s \times K}$
- 2: Initialize sketches: $X_{\text{range}} \leftarrow \mathbf{0}_{n \times q}$, $X_{\text{corange}} \leftarrow \mathbf{0}_{q \times K}$, $X_{\text{core}} \leftarrow \mathbf{0}_{s \times s}$
- 3: **for** $k = 1$ to K **do**
- 4: Receive new data vector: \mathbf{x}_k
- 5: Update sketches: $\triangleright (i, j)$ is entry at row i and column j , $(:)$ are all entries in that dimension
- $$X_{\text{range}} \leftarrow X_{\text{range}} + \mathbf{x}_k \Omega^T(k, :), \quad X_{\text{corange}}(:, k) \leftarrow X_{\text{corange}}(:, k) + \Upsilon \mathbf{x}_k, \quad X_{\text{core}} \leftarrow X_{\text{core}} + (\Xi \mathbf{x}_k) \Psi^T(k, :)$$
- 6: **end for**
- 7: Compute the core matrix $\mathbf{C} \in \mathbb{R}^{s \times s}$: $\triangleright \dagger$: Moore-Penrose pseudo-inverse
- $$\mathbf{Q}_{\text{range}} \mathbf{R}_{\text{range}} \leftarrow \text{qr}(X_{\text{range}}), \quad \mathbf{Q}_{\text{corange}} \mathbf{R}_{\text{corange}} \leftarrow \text{qr}(X_{\text{corange}}^T), \quad \mathbf{C} \leftarrow (\Xi \mathbf{Q}_{\text{range}})^\dagger X_{\text{core}} ((\Psi \mathbf{Q}_{\text{corange}})^\dagger)^T$$
- 8: Compute SVD of the core matrix: $\mathbf{V}_c \Sigma_c \mathbf{W}_c^T \leftarrow \text{svd}(\mathbf{C})$
- 9: Form SVD of \mathbf{X} : $\mathbf{V}_r \leftarrow \mathbf{Q}_{\text{range}} \mathbf{V}_c(:, 1:r)$, $\Sigma_r \leftarrow \Sigma_c(1:r, 1:r)$, $\mathbf{W}_r \leftarrow \mathbf{Q}_{\text{corange}} \mathbf{W}_c(:, 1:r)$
- 10: **Return:** \mathbf{V}_r , Σ_r , \mathbf{W}_r

B. Recursive Least-Squares Algorithms

Algorithm 3 RLS Algorithm

Require: Tikhonov matrix $\Gamma = \Gamma^T > 0$

- 1: $\mathbf{P}_0 = \Gamma^{-1}$ \triangleright Initialize inverse correlation matrix
- 2: $\mathbf{O}_0 = \mathbf{0}_{d \times r}$ \triangleright Initialize operator matrix
- 3: **for** $k = 1, 2, 3, \dots, K$ **do**
- 4: Receive new data: $\mathbf{d}_k, \mathbf{r}_k$
- 5: $c_k = (1 + \mathbf{d}_k \mathbf{P}_{k-1} \mathbf{d}_k^T)^{-1}$ \triangleright Compute conversion factor
- 6: $\mathbf{g}_k = \mathbf{P}_{k-1} \mathbf{d}_k^T c_k$ \triangleright Update Kalman gain
- 7: $\mathbf{P}_k = \mathbf{P}_{k-1} - \mathbf{g}_k \mathbf{g}_k^T c_k^{-1}$ \triangleright Update inverse correlation matrix
- 8: $\xi_k^- = \mathbf{r}_k - \mathbf{d}_k \mathbf{O}_{k-1}$ \triangleright Compute *a priori* error
- 9: $\mathbf{O}_k = \mathbf{O}_{k-1} + \mathbf{g}_k \xi_k^-$ \triangleright Update operator matrix
- 10: **end for**
- 11: **Return:** \mathbf{O}_k

Algorithm 4 Inverse QR-Decomposition RLS Algorithm

Require: Tikhonov matrix $\Gamma = \Gamma^\top > 0$

1: Initialize $\mathbf{P}_0^{1/2} \leftarrow \Gamma^{-1/2}$ ▷ Cholesky decomposition of inverse correlation matrix

2: Initialize $\mathbf{O}_0 \leftarrow \mathbf{0}_{d \times r}$ ▷ Operator estimate

3: **for** $k = 1$ to K **do**

4: Receive new data: $\mathbf{d}_k, \mathbf{r}_k$

5: Form tranposed pre-array:

$$\mathcal{A}_k^\top = \begin{bmatrix} 1 & \mathbf{0}_{1 \times d} \\ \mathbf{P}_{k-1}^{\top/2} \mathbf{d}_k^\top & \mathbf{P}_{k-1}^{\top/2} \end{bmatrix}$$

6: Perform QR decomposition (or Givens rotations): $\Theta_k \mathcal{B}_k^\top \leftarrow \text{qr}(\mathcal{A}_k^\top)$

7: Extract updated quantities:

$$c_k^{-1/2} \leftarrow \mathcal{B}_k^\top(1, 1), \quad \mathbf{g}_k c_k^{-1/2} \leftarrow \mathcal{B}_k^\top(1, 2 : d+1), \quad \mathbf{P}_k^{1/2} \leftarrow (\mathcal{B}_k^\top(2 : d+1, 2 : d+1))^\top$$

8: Compute the a priori error: $\xi_k^- \leftarrow \mathbf{r}_k - \mathbf{d}_k \mathbf{O}_{k-1}$

9: Update the operator estimate:

$$\mathbf{O}_k = \mathbf{O}_{k-1} + (\mathbf{g}_k c_k^{-1/2}) (c_k^{-1/2})^{-1} \xi_k^- = \mathbf{O}_{k-1} + \mathbf{g}_k \xi_k^-$$

10: **end for**

11: **Return:** \mathbf{O}_K

C. Proof of Theorem 3.3

This section provides the proof of Theorem 3.3, which establishes error bounds for operators learned via streaming SVD within the proposed Streaming OpInf paradigms. The theorem quantifies how errors in the streaming SVD, relative to the batch SVD, propagate through the data matrices \mathbf{D} and \mathbf{R} into the learned operators. We first prove the supporting Lemmas 3.1 and 3.2, then combine these results to establish the theorem.

C.1. Proof of Lemma 3.1

The proof relies on the following classical perturbation result for pseudoinverses.

Lemma C.1 (Theorem 4.1 of [128]). *Let $\mathbf{A}, \mathbf{B} \in \mathbb{R}^{m \times n}$ with $\text{rank}(\mathbf{A}) = \text{rank}(\mathbf{B}) = \min\{m, n\}$. Then*

$$\|\mathbf{A}^\dagger - \mathbf{B}^\dagger\|_2 \leq \alpha \|\mathbf{A}^\dagger\|_2 \|\mathbf{B}^\dagger\|_2 \|\mathbf{A} - \mathbf{B}\|_2,$$

where $\alpha = \sqrt{2}$ if $m \neq n$ and $\alpha = 1$ if $m = n$.

Proof of Lemma 3.1. Let the data matrices $\bar{\mathbf{D}}$ and $\bar{\mathbf{R}}$ be defined as in (7), and define the perturbed data matrices as $\tilde{\mathbf{D}} = \bar{\mathbf{D}} + [\mathbf{E}_D^\top, \mathbf{0}_{d \times d}]^\top$ and $\tilde{\mathbf{R}} = \bar{\mathbf{R}} + [\mathbf{E}_R^\top, \mathbf{0}_{r \times d}]^\top$. The corresponding LS solutions are $\mathbf{O} = \bar{\mathbf{D}}^\dagger \bar{\mathbf{R}}$ and $\tilde{\mathbf{O}} = \tilde{\mathbf{D}}^\dagger \tilde{\mathbf{R}}$, respectively. Adding and subtracting $\tilde{\mathbf{D}}^\dagger \tilde{\mathbf{R}}$ yields

$$\|\mathbf{O} - \tilde{\mathbf{O}}\|_F = \|\bar{\mathbf{D}}^\dagger \bar{\mathbf{R}} - \tilde{\mathbf{D}}^\dagger \tilde{\mathbf{R}}\|_F = \|\bar{\mathbf{D}}^\dagger \bar{\mathbf{R}} - \bar{\mathbf{D}}^\dagger \tilde{\mathbf{R}} + \bar{\mathbf{D}}^\dagger \tilde{\mathbf{R}} - \tilde{\mathbf{D}}^\dagger \tilde{\mathbf{R}}\|_F \leq \|\bar{\mathbf{D}}^\dagger(\bar{\mathbf{R}} - \tilde{\mathbf{R}})\|_F + \|(\bar{\mathbf{D}}^\dagger - \tilde{\mathbf{D}}^\dagger)\tilde{\mathbf{R}}\|_F,$$

where the inequality follows from the triangle inequality. Applying submultiplicativity of the mixed matrix norms [129] to each term gives

$$\|\mathbf{O} - \tilde{\mathbf{O}}\|_F \leq \|\bar{\mathbf{D}}^\dagger\|_2 \|\bar{\mathbf{R}} - \tilde{\mathbf{R}}\|_F + \|\bar{\mathbf{D}}^\dagger - \tilde{\mathbf{D}}^\dagger\|_2 \|\tilde{\mathbf{R}}\|_F.$$

Applying Lemma C.1 to the second term and substituting $\|\bar{\mathbf{R}} - \tilde{\mathbf{R}}\|_F = \|\mathbf{E}_R\|_F$ and $\|\bar{\mathbf{D}} - \tilde{\mathbf{D}}\|_2 = \|\mathbf{E}_D\|_2$ completes the proof. Note that $\|[\mathbf{E}_R^\top, \mathbf{0}_{r \times d}]^\top\|_F = \|\mathbf{E}_R\|_F$ and $\|[\mathbf{E}_D^\top, \mathbf{0}_{d \times d}]^\top\|_2 = \|\mathbf{E}_D\|_2$. \square

C.2. Proof of Lemma 3.2

Before proceeding, we introduce notation for the full-state data matrix

$$\mathbb{D} = \begin{bmatrix} \mathbf{X}^\top & (\mathbf{X} \odot \mathbf{X})^\top & \mathbf{U}^\top & \mathbf{1}_K \end{bmatrix} \in \mathbb{R}^{K \times (n+n^2+m+1)}.$$

For the projection-based paradigms, the data matrices $\bar{\mathbf{D}}$ and $\tilde{\mathbf{D}}$ can be expressed as

$$\bar{\mathbf{D}} = [(\mathbb{D}\mathbb{V}_r)^\top, \mathbf{\Gamma}^{1/2}]^\top \quad \text{and} \quad \tilde{\mathbf{D}} = [(\mathbb{D}\tilde{\mathbb{V}}_r)^\top, \mathbf{\Gamma}^{1/2}]^\top,$$

where

$$\mathbb{V}_r = \begin{bmatrix} \mathbf{V}_r & 0 & 0 & 0 \\ 0 & \mathbf{V}_r \otimes \mathbf{V}_r & 0 & 0 \\ 0 & 0 & \mathbf{I}_m & 0 \\ 0 & 0 & 0 & 1 \end{bmatrix}, \quad \tilde{\mathbb{V}}_r = \begin{bmatrix} \tilde{\mathbf{V}}_r & 0 & 0 & 0 \\ 0 & \tilde{\mathbf{V}}_r \otimes \tilde{\mathbf{V}}_r & 0 & 0 \\ 0 & 0 & \mathbf{I}_m & 0 \\ 0 & 0 & 0 & 1 \end{bmatrix}.$$

The matrices $\mathbb{V}_r, \tilde{\mathbb{V}}_r \in \mathbb{R}^{(n+n^2+m+1) \times (r+r^2+m+1)}$ have orthonormal columns.

Proof of Lemma 3.2. The bound $|\sigma_j - \tilde{\sigma}_j| \leq \varepsilon$ for all $j = 1, \dots, r$ follows directly from Weyl's inequality [130, Cor. 8.6.2] under the assumption $\|\mathbf{X} - \tilde{\mathbf{X}}\|_2 \leq \varepsilon$.

Projection paradigms (iSVD-Project-LS/RLS). We first bound the perturbation in the data matrix \mathbf{D} . By submultiplicativity,

$$\|\mathbf{E}_D\|_2 = \|\mathbb{D}(\mathbb{V}_r - \tilde{\mathbb{V}}_r)\|_2 \leq \|\mathbb{D}\|_2 \|\mathbb{V}_r - \tilde{\mathbb{V}}_r\|_2. \quad (\text{C.1})$$

The block-diagonal structure of $\mathbb{V}_r - \tilde{\mathbb{V}}_r$ implies that its norm is the maximum norm of a diagonal block

$$\|\mathbb{V}_r - \tilde{\mathbb{V}}_r\|_2 = \max\{\|\mathbb{V}_r - \tilde{\mathbb{V}}_r\|_2, \|\mathbb{V}_r \otimes \mathbb{V}_r - \tilde{\mathbb{V}}_r \otimes \tilde{\mathbb{V}}_r\|_2\}.$$

By assumption, $\|\mathbf{v}_j - \tilde{\mathbf{v}}_j\|_2 \leq \varepsilon_{v,j}$ for each j , so

$$\|\mathbb{V}_r - \tilde{\mathbb{V}}_r\|_F \leq \left(\sum_{j=1}^r \varepsilon_{v,j}^2 \right)^{1/2} = \tau_v.$$

Since the Frobenius norm dominates the spectral norm, $\|\mathbb{V}_r - \tilde{\mathbb{V}}_r\|_2 \leq \tau_v$.

For the Kronecker product term, we add and subtract $\tilde{\mathbb{V}}_r \otimes \mathbb{V}_r$ to obtain

$$\mathbb{V}_r \otimes \mathbb{V}_r - \tilde{\mathbb{V}}_r \otimes \tilde{\mathbb{V}}_r = (\mathbb{V}_r - \tilde{\mathbb{V}}_r) \otimes \mathbb{V}_r + \tilde{\mathbb{V}}_r \otimes (\mathbb{V}_r - \tilde{\mathbb{V}}_r).$$

Applying the triangle inequality and the spectral norm property of Kronecker products [131, Thm. 8], namely $\|\mathbf{A} \otimes \mathbf{B}\|_2 = \|\mathbf{A}\|_2 \|\mathbf{B}\|_2$, yields

$$\|\mathbb{V}_r \otimes \mathbb{V}_r - \tilde{\mathbb{V}}_r \otimes \tilde{\mathbb{V}}_r\|_2 \leq \|\mathbb{V}_r - \tilde{\mathbb{V}}_r\|_2 \|\mathbb{V}_r\|_2 + \|\tilde{\mathbb{V}}_r\|_2 \|\mathbb{V}_r - \tilde{\mathbb{V}}_r\|_2 = 2\|\mathbb{V}_r - \tilde{\mathbb{V}}_r\|_2 \leq 2\tau_v,$$

where we used $\|\mathbb{V}_r\|_2 = \|\tilde{\mathbb{V}}_r\|_2 = 1$ since both matrices have orthonormal columns.

It remains to bound $\|\mathbb{D}\|_2$. Assuming bounded inputs $\|\mathbf{U}\|_\infty < \eta$ for some $\eta > 0$, we have

$$\|\mathbb{D}\|_2^2 \leq \|\mathbf{X}\|_2^2 + \|\mathbf{X} \odot \mathbf{X}\|_2^2 + \eta^2 + K.$$

The Khatri–Rao product satisfies $(\mathbf{X} \odot \mathbf{X})^\top (\mathbf{X} \odot \mathbf{X}) = (\mathbf{X}^\top \mathbf{X}) \circ (\mathbf{X}^\top \mathbf{X})$, where \circ denotes the Hadamard product. By [132, Thm. 5.5.1], $\sigma_1((\mathbf{X}^\top \mathbf{X}) \circ (\mathbf{X}^\top \mathbf{X})) \leq \sigma_1(\mathbf{X}^\top \mathbf{X})^2 = \|\mathbf{X}\|_2^4$. Thus,

$$\|\mathbb{D}\|_2 \leq (\sigma_1^2 + \sigma_1^4 + \eta^2 + K)^{1/2} =: \beta'_1,$$

where $\sigma_1 = \|\mathbf{X}\|_2$. Substituting into (C.1) gives $\|\mathbf{E}_D\|_2 \leq 2\beta'_1 \tau_v$. Note that $\beta'_1 = \beta_1 / (2\sqrt{\min\{n, K\}})$ using the constant β_1 defined in (C.6), and hence, $\|\mathbf{E}_D\|_2 \leq \beta_1 \tau_v / \sqrt{\min\{n, K\}}$.

For the right-hand side perturbation, we have $\mathbf{E}_R = (\mathbf{V}_r - \widetilde{\mathbf{V}}_r)^\top \dot{\mathbf{X}}$. Given the polynomial structure of the underlying dynamical system (1), the vector field is continuously differentiable and hence L_f -Lipschitz continuous for some $L_f > 0$. This property can be used to bound $\|\dot{\mathbf{X}}\|_2$ in general settings. However, to obtain bounds that are directly comparable across paradigms and more readily interpretable, we assume the time-derivative data is computed via finite-difference approximations, i.e., $\dot{\mathbf{X}} = \mathbf{X}\Delta_K$, where $\Delta_K \in \mathbb{R}^{K \times K}$ is the finite-difference operator matrix defined in Section 3.1. This assumption is reasonable in practice, as time-derivative data is often unavailable and must be approximated from state snapshots. Under this assumption,

$$\|\mathbf{E}_R\|_F = \|(\mathbf{V}_r - \widetilde{\mathbf{V}}_r)^\top \mathbf{X}\Delta_K\|_F \leq \|\mathbf{V}_r - \widetilde{\mathbf{V}}_r\|_F \|\mathbf{X}\|_2 \|\Delta_K\|_2 \leq \sigma_1 \|\Delta_K\|_2 \tau_v.$$

Reformulation paradigms (iSVD-LS/RLS). For these paradigms, the data matrix perturbation takes the form

$$\mathbf{E}_D = \begin{bmatrix} \mathbf{W}_r \Sigma_r - \widetilde{\mathbf{W}}_r \widetilde{\Sigma}_r & (\mathbf{W}_r \Sigma_r) \otimes (\mathbf{W}_r \Sigma_r) - (\widetilde{\mathbf{W}}_r \widetilde{\Sigma}_r) \otimes (\widetilde{\mathbf{W}}_r \widetilde{\Sigma}_r) & \mathbf{0} & \mathbf{0} \end{bmatrix}.$$

The block structure implies

$$\|\mathbf{E}_D\|_2^2 \leq \|\mathbf{W}_r \Sigma_r - \widetilde{\mathbf{W}}_r \widetilde{\Sigma}_r\|_2^2 + \|(\mathbf{W}_r \Sigma_r) \otimes (\mathbf{W}_r \Sigma_r) - (\widetilde{\mathbf{W}}_r \widetilde{\Sigma}_r) \otimes (\widetilde{\mathbf{W}}_r \widetilde{\Sigma}_r)\|_2^2. \quad (\text{C.2})$$

For the first term, we add and subtract $\widetilde{\mathbf{W}}_r \widetilde{\Sigma}_r$:

$$\mathbf{W}_r \Sigma_r - \widetilde{\mathbf{W}}_r \widetilde{\Sigma}_r = (\mathbf{W}_r - \widetilde{\mathbf{W}}_r) \Sigma_r + \widetilde{\mathbf{W}}_r (\Sigma_r - \widetilde{\Sigma}_r).$$

Applying the triangle inequality, submultiplicativity, and the bounds $\|\mathbf{w}_j - \widetilde{\mathbf{w}}_j\|_2 \leq \varepsilon_{w,j}$ and $|\sigma_j - \widetilde{\sigma}_j| \leq \varepsilon$ yields

$$\|\mathbf{W}_r \Sigma_r - \widetilde{\mathbf{W}}_r \widetilde{\Sigma}_r\|_F \leq \|\Sigma_r\|_2 \|\mathbf{W}_r - \widetilde{\mathbf{W}}_r\|_F + \|\widetilde{\mathbf{W}}_r\|_2 \|\Sigma_r - \widetilde{\Sigma}_r\|_F \leq \sigma_1 \tau_w + \sqrt{r} \varepsilon = \phi_w,$$

where $\tau_w = (\sum_{j=1}^r \varepsilon_{w,j}^2)^{1/2}$ and we used $\|\widetilde{\mathbf{W}}_r\|_2 = 1$. Since the Frobenius norm dominates the spectral norm, $\|\mathbf{W}_r \Sigma_r - \widetilde{\mathbf{W}}_r \widetilde{\Sigma}_r\|_2 \leq \phi_w$.

For the Kronecker product term in (C.2), we proceed analogously to the projection case. Adding and subtracting $(\widetilde{\mathbf{W}}_r \widetilde{\Sigma}_r) \otimes (\mathbf{W}_r \Sigma_r)$ and applying the triangle inequality and [131, Thm. 8] gives

$$\|(\mathbf{W}_r \Sigma_r) \otimes (\mathbf{W}_r \Sigma_r) - (\widetilde{\mathbf{W}}_r \widetilde{\Sigma}_r) \otimes (\widetilde{\mathbf{W}}_r \widetilde{\Sigma}_r)\|_2 \leq (\|\mathbf{W}_r \Sigma_r\|_2 + \|\widetilde{\mathbf{W}}_r \widetilde{\Sigma}_r\|_2) \|\mathbf{W}_r \Sigma_r - \widetilde{\mathbf{W}}_r \widetilde{\Sigma}_r\|_2.$$

Since $\|\mathbf{W}_r \Sigma_r\|_2 = \sigma_1$ and $\|\widetilde{\mathbf{W}}_r \widetilde{\Sigma}_r\|_2 = \max_j \widetilde{\sigma}_j \leq \sigma_1 + \varepsilon$, we obtain

$$\|(\mathbf{W}_r \Sigma_r) \otimes (\mathbf{W}_r \Sigma_r) - (\widetilde{\mathbf{W}}_r \widetilde{\Sigma}_r) \otimes (\widetilde{\mathbf{W}}_r \widetilde{\Sigma}_r)\|_2 \leq (2\sigma_1 + \varepsilon) \phi_w.$$

Substituting into (C.2) along with $\sqrt{1 + (2\sigma_1 + \varepsilon)^2} = \beta_2 / [\sqrt{r}(\sigma_1 + \varepsilon)]$ from Equation (C.7) and expanding ϕ_w yields

$$\|\mathbf{E}_D\|_2 \leq [\phi_w^2 + (2\sigma_1 + \varepsilon)^2 \phi_w^2]^{1/2} = \phi_w \sqrt{1 + (2\sigma_1 + \varepsilon)^2} = \sigma_1 \beta_2 \tau_w / [\sqrt{r}(\sigma_1 + \varepsilon)] + \beta_2 \varepsilon / (\sigma_1 + \varepsilon).$$

For the right-hand side perturbation, we have $\mathbf{R} = \Delta_K^\top \mathbf{W}_r \Sigma_r$ and $\widetilde{\mathbf{R}} = \Delta_K^\top \widetilde{\mathbf{W}}_r \widetilde{\Sigma}_r$, so

$$\|\mathbf{E}_R\|_F = \|\Delta_K^\top (\mathbf{W}_r \Sigma_r - \widetilde{\mathbf{W}}_r \widetilde{\Sigma}_r)\|_F \leq \|\Delta_K\|_2 \|\mathbf{W}_r \Sigma_r - \widetilde{\mathbf{W}}_r \widetilde{\Sigma}_r\|_F \leq \|\Delta_K\|_2 \phi_w = \sigma_1 \|\Delta_K\|_2 \tau_w + \sqrt{r} \|\Delta_K\|_2 \varepsilon. \quad \square$$

C.3. Proof of Theorem 3.3

To apply Lemma 3.1, we require bounds on $\|\bar{\mathbf{D}}^\dagger\|_2$, $\|\widetilde{\mathbf{D}}^\dagger\|_2$, and $\|\bar{\mathbf{R}}\|_F$. We begin with a standard result relating the pseudoinverse norm to the minimum singular value.

Lemma C.2 (Norm of the pseudoinverse). *For any $\mathbf{A} \in \mathbb{R}^{m \times n}$, we have $\|\mathbf{A}^\dagger\|_2 = \sigma_{\min}(\mathbf{A})^{-1}$, where $\sigma_{\min}(\mathbf{A})$ denotes the smallest nonzero singular value of \mathbf{A} .*

Proof. Let $\mathbf{B} = \mathbf{A}^\dagger$. Since \mathbf{AB} is an orthogonal projector onto $\text{range}(\mathbf{A})$, we have $\mathbf{AB}\mathbf{x} \perp (\mathbf{I} - \mathbf{AB})\mathbf{x}$ for any $\mathbf{x} \in \mathbb{R}^n$. Therefore,

$$\|\mathbf{B}\|_2 = \max_{\mathbf{x} \neq 0} \frac{\|\mathbf{B}\mathbf{x}\|_2}{\|\mathbf{x}\|_2} = \max_{\mathbf{x} \neq 0} \frac{\|\mathbf{B}\mathbf{x}\|_2}{\|\mathbf{AB}\mathbf{x} + (\mathbf{I} - \mathbf{AB})\mathbf{x}\|_2} = \max_{\mathbf{B}\mathbf{x} \neq 0} \frac{\|\mathbf{B}\mathbf{x}\|_2}{\|\mathbf{AB}\mathbf{x} + (\mathbf{I} - \mathbf{AB})\mathbf{x}\|_2} \leq \max_{\mathbf{B}\mathbf{x} \neq 0} \frac{\|\mathbf{B}\mathbf{x}\|_2}{\|\mathbf{AB}\mathbf{x}\|_2},$$

where the inequality follows from orthogonality. Substituting $\mathbf{y} = \mathbf{B}\mathbf{x}$ and noting that \mathbf{y} ranges over $\text{range}(\mathbf{B}) = \text{range}(\mathbf{A}^\top)$ gives

$$\|\mathbf{B}\|_2 \leq \max_{\mathbf{y} \in \text{range}(\mathbf{A}^\top), \mathbf{y} \neq 0} \frac{\|\mathbf{y}\|_2}{\|\mathbf{Ay}\|_2} = \left(\min_{\mathbf{y} \in \text{range}(\mathbf{A}^\top), \mathbf{y} \neq 0} \frac{\|\mathbf{Ay}\|_2}{\|\mathbf{y}\|_2} \right)^{-1} = \sigma_{\min}(\mathbf{A})^{-1}.$$

Equality is attained by taking \mathbf{x} in the direction of the right singular vector corresponding to $\sigma_{\min}(\mathbf{A})$. \square

Bounds on $\|\tilde{\mathbf{R}}\|_F$. For the projection-based paradigms, $\tilde{\mathbf{R}} = \tilde{\mathbf{V}}_r^\top \dot{\mathbf{X}}$. Under the finite-difference assumption $\dot{\mathbf{X}} = \mathbf{X}\Delta_K$,

$$\|\tilde{\mathbf{R}}\|_F \leq \|\tilde{\mathbf{V}}_r\|_2 \|\mathbf{X}\|_F \|\Delta_K\|_2 \leq \sigma_1 \sqrt{\min\{n, K\}} \|\Delta_K\|_2, \quad (\text{C.3})$$

where we used $\|\tilde{\mathbf{V}}_r\|_2 = 1$ and $\|\mathbf{X}\|_F \leq \sigma_1 \sqrt{\min\{n, K\}}$.

For the reformulation paradigms, $\tilde{\mathbf{R}} = \Delta_K^\top \tilde{\mathbf{W}}_r \tilde{\Sigma}_r$, so

$$\|\tilde{\mathbf{R}}\|_F \leq \|\Delta_K\|_2 \|\tilde{\Sigma}_r\|_F, \quad (\text{C.4})$$

since $\tilde{\mathbf{W}}_r$ has orthonormal columns. To bound $\|\tilde{\Sigma}_r\|_F$, let $\sigma = [\sigma_1, \dots, \sigma_r]^\top$ and $\delta = [\delta_1, \dots, \delta_r]^\top$ where $\delta_j = \tilde{\sigma}_j - \sigma_j$ satisfies $|\delta_j| \leq \varepsilon$. Then using the inner product operator $\langle \cdot, \cdot \rangle$ we have

$$\|\tilde{\Sigma}_r\|_F^2 = \sum_{j=1}^r (\sigma_j + \delta_j)^2 = \|\Sigma_r\|_F^2 + 2\langle \sigma, \delta \rangle + \|\delta\|_2^2.$$

The Cauchy-Schwarz inequality gives $|\langle \sigma, \delta \rangle| \leq \|\sigma\|_2 \|\delta\|_2 \leq \|\Sigma_r\|_F \cdot \sqrt{r}\varepsilon$, and $\|\delta\|_2 \leq \sqrt{r}\varepsilon$. Therefore,

$$\|\tilde{\Sigma}_r\|_F \leq \|\Sigma_r\|_F + \sqrt{r}\varepsilon \leq \sigma_1 \sqrt{r} + \sqrt{r}\varepsilon = \sqrt{r}(\sigma_1 + \varepsilon).$$

Substituting into (C.4) yields

$$\|\tilde{\mathbf{R}}\|_F \leq \|\Delta_K\|_2 \sqrt{r}(\sigma_1 + \varepsilon). \quad (\text{C.5})$$

Bounds on $\|\bar{\mathbf{D}}^\dagger\|_2$ and $\|\tilde{\mathbf{D}}^\dagger\|_2$. In OpInf, the data matrix \mathbf{D} is commonly ill-conditioned due to linear dependence among columns arising from small time-step sizes and/or the quadratic nonlinearity [1, 55]. When the state data exhibits rapid spectral decay, the quadratic terms amplify this effect by squaring the singular values, further reducing $\sigma_{\min}(\mathbf{D})$. Consequently, it is often necessary to choose the regularization parameter such that $\sqrt{\gamma_{\min}} = \min_j \sqrt{\gamma_j} \gg \sigma_{\min}(\mathbf{D})$. With a similar reasoning on $\bar{\mathbf{D}}$, we suppose the perturbed minimum singular value satisfies $\sqrt{\gamma_{\min}} \gg \sigma_{\min}(\mathbf{D} + \mathbf{E}_D)$.

Under these assumptions, Lemma C.2 gives

$$\|\bar{\mathbf{D}}^\dagger\|_2 = \sigma_{\min}(\bar{\mathbf{D}})^{-1} = [\sigma_{\min}(\mathbf{D})^2 + \gamma_{\min}]^{-1/2} \approx \gamma_{\min}^{-1/2},$$

and we similarly have

$$\|\tilde{\mathbf{D}}^\dagger\|_2 = [\sigma_{\min}(\mathbf{D} + \mathbf{E}_D)^2 + \gamma_{\min}]^{-1/2} \approx \gamma_{\min}^{-1/2}.$$

Completing the proof. Substituting the bounds from Lemma 3.2 and the estimates above into Lemma 3.1, we obtain for the projection paradigms (iSVD-Project-LS/RLS):

$$\|\mathbf{O} - \tilde{\mathbf{O}}\|_F \leq \frac{\alpha}{\gamma_{\min}} \cdot 2\beta'_1 \tau_v \cdot \sigma_1 \sqrt{\min\{n, K\}} \|\Delta_K\|_2 + \frac{1}{\sqrt{\gamma_{\min}}} \cdot \sigma_1 \|\Delta_K\|_2 \tau_v = \frac{\sigma_1 \|\Delta_K\|_2}{\sqrt{\gamma_{\min}}} \tau_v \left(1 + \frac{\alpha \beta_1}{\sqrt{\gamma_{\min}}} \right), \quad (\text{C.6})$$

where $\beta_1 = 2\beta'_1 \sqrt{\min\{n, K\}}$.

For the reformulation paradigms (iSVD-LS/RLS), substituting the bounds yields

$$\|\mathbf{O} - \tilde{\mathbf{O}}\|_F \leq \frac{\alpha}{\gamma_{\min}} \cdot \phi_w \sqrt{1 + (2\sigma_1 + \varepsilon)^2} \cdot \|\Delta_K\|_2 \sqrt{r}(\sigma_1 + \varepsilon) + \frac{1}{\sqrt{\gamma_{\min}}} \cdot \|\Delta_K\|_2 \phi_w.$$

Expanding $\phi_w = \sigma_1 \tau_w + \sqrt{r}\varepsilon$ and collecting terms gives

$$\|\mathbf{O} - \tilde{\mathbf{O}}\|_F \leq \frac{\sigma_1 \|\Delta_K\|_2}{\sqrt{\gamma_{\min}}} \tau_w \left(1 + \frac{\alpha \beta_2}{\sqrt{\gamma_{\min}}} \right) + \frac{(\alpha \beta_2 + \sqrt{\gamma_{\min}}) \sqrt{r} \|\Delta_K\|_2}{\gamma_{\min}} \varepsilon, \quad (\text{C.7})$$

where $\beta_2 = \sqrt{r}(\sigma_1 + \varepsilon) \sqrt{1 + (2\sigma_1 + \varepsilon)^2}$ and both β_1, β_2 have order $O(\sigma_1^2)$ if σ_1 dominates. This completes the proof.

D. Additional Turbulent Channel Flow Field Predictions

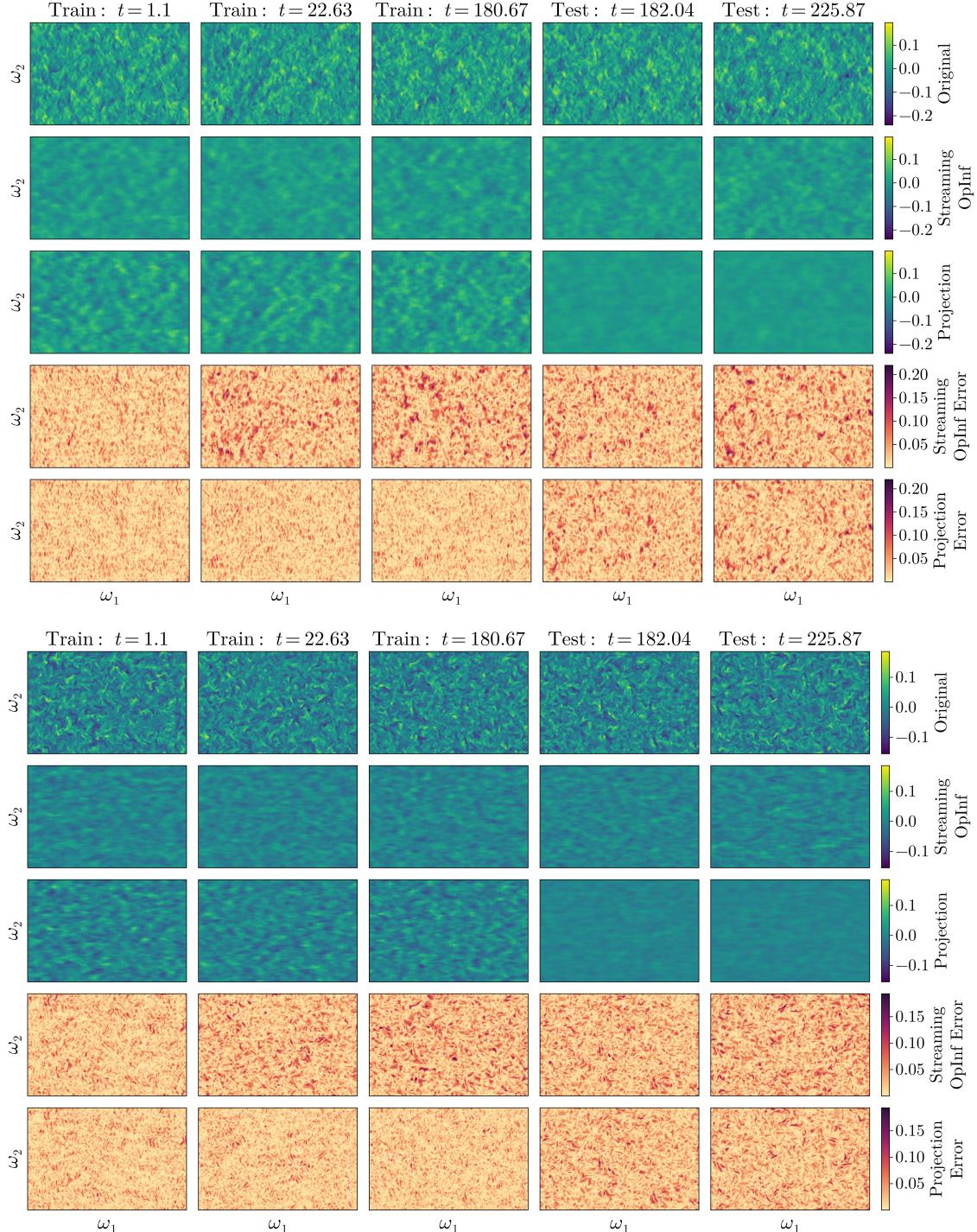


Figure D.13: Comparison of 2D slices of the 3D turbulent channel flow field predictions for the **(top)** spanwise and **(bottom)** wall-normal velocity components. First row is the original data, the second row is the prediction from Streaming-OptInf with $r = 300$, the third row is the projection result from POD with $r = 300$, and the last two rows is the absolute error between the original data and the predictions.

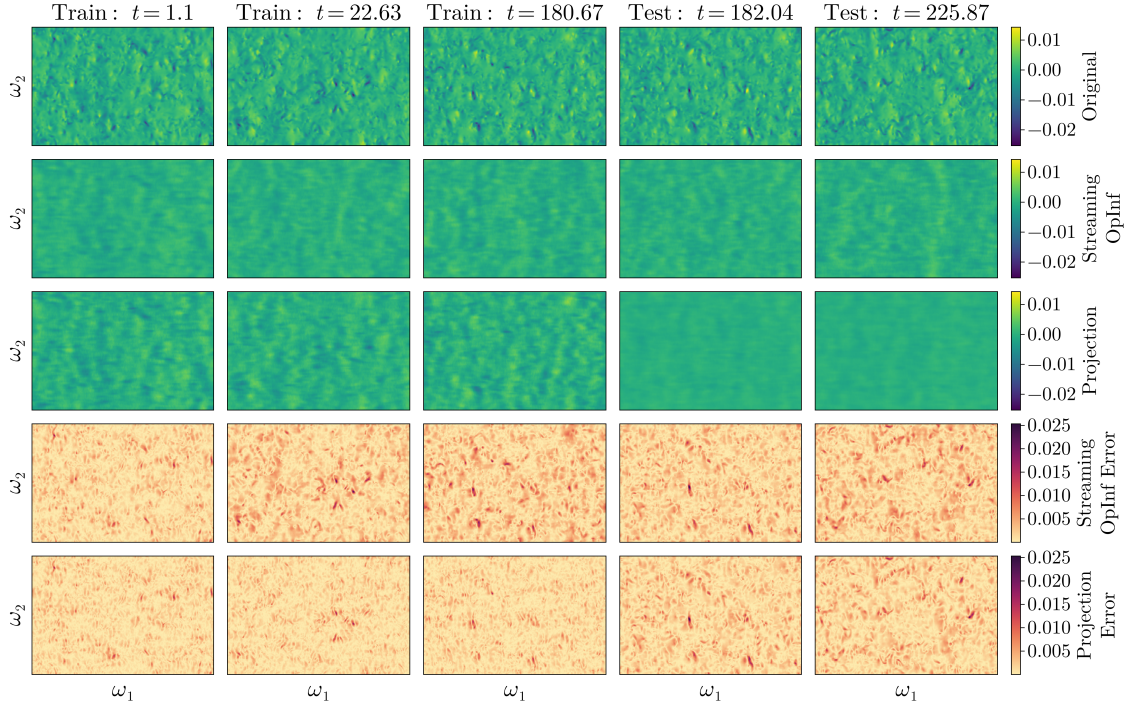


Figure D.14: Comparison of 2D slices of the 3D turbulent channel flow field predictions the **pressure field**. First row is the original data, the second row is the prediction from Streaming-OpInf with $r = 300$, the third row is the projection result from POD with $r = 300$, and the last two rows are the absolute error between the original data and the prediction from Streaming-OpInf and POD, respectively.

References

- [1] B. Peherstorfer, K. Willcox, Data-driven operator inference for nonintrusive projection-based model reduction, *Computer Methods in Applied Mechanics and Engineering* 306 (2016) 196–215. [doi:10.1016/j.cma.2016.03.025](https://doi.org/10.1016/j.cma.2016.03.025).
- [2] B. Kramer, B. Peherstorfer, K. E. Willcox, Learning Nonlinear Reduced Models from Data with Operator Inference, *Annual Review of Fluid Mechanics* 56 (1) (2024) null. [doi:10.1146/annurev-fluid-121021-025220](https://doi.org/10.1146/annurev-fluid-121021-025220).
- [3] P. Benner, S. Gugercin, K. Willcox, A Survey of Projection-Based Model Reduction Methods for Parametric Dynamical Systems, *SIAM Review* 57 (4) (2015) 483–531. [doi:10.1137/130932715](https://doi.org/10.1137/130932715).
- [4] R. Geelen, S. Wright, K. Willcox, Operator inference for non-intrusive model reduction with quadratic manifolds, *Computer Methods in Applied Mechanics and Engineering* 403 (2023) 115717. [doi:10.1016/j.cma.2022.115717](https://doi.org/10.1016/j.cma.2022.115717).
- [5] R. Geelen, L. Balzano, S. Wright, K. Willcox, Learning physics-based reduced-order models from data using nonlinear manifolds (Feb. 2024). [arXiv:2308.02802](https://arxiv.org/abs/2308.02802), [doi:10.48550/arXiv.2308.02802](https://doi.org/10.48550/arXiv.2308.02802).
- [6] P. Schwerdtner, P. Mohan, J. Bessac, M. T. H. de Frahan, B. Peherstorfer, Operator inference aware quadratic manifolds with isotropic reduced coordinates for nonintrusive model reduction, *arXiv preprint arXiv:2507.20463* (2025).
- [7] A. Padovan, B. Vollmer, D. J. Bodony, Data-Driven Model Reduction via Non-intrusive Optimization of Projection Operators and Reduced-Order Dynamics, *SIAM Journal on Applied Dynamical Systems* 23 (4) (2024) 3052–3076. [doi:10.1137/24M1628414](https://doi.org/10.1137/24M1628414).
- [8] S. A. McQuarrie, C. Huang, K. E. Willcox, Data-driven reduced-order models via regularised Operator Inference for a single-injector combustion process, *Journal of the Royal Society of New Zealand* 51 (2) (2021) 194–211. [doi:10.1080/03036758.2020.1863237](https://doi.org/10.1080/03036758.2020.1863237).
- [9] N. Sawant, B. Kramer, B. Peherstorfer, Physics-informed regularization and structure preservation for learning stable reduced models from data with operator inference, *Computer Methods in Applied Mechanics and Engineering* 404 (2023) 115836. [doi:10.1016/j.cma.2022.115836](https://doi.org/10.1016/j.cma.2022.115836).
- [10] P. den Boef, D. Manvelyan, J. Maubach, W. Schilders, N. van de Wouw, Stable Sparse Operator Inference for Nonlinear Structural Dynamics, *arXiv preprint arXiv:2407.21672* (Jul. 2024). [arXiv:2407.21672](https://arxiv.org/abs/2407.21672), [doi:10.48550/arXiv.2407.21672](https://doi.org/10.48550/arXiv.2407.21672).
- [11] E. Danis, D. Truong, K. Ø. Rasmussen, B. S. Alexandrov, Tensor-Train Operator Inference, *arXiv preprint arXiv:2509.08071* (Sep. 2025). [arXiv:2509.08071](https://arxiv.org/abs/2509.08071), [doi:10.48550/arXiv.2509.08071](https://doi.org/10.48550/arXiv.2509.08071).

[12] N. Aretz, K. Willcox, Nested Operator Inference for Adaptive Data-Driven Learning of Reduced-order Models, arXiv preprint arXiv:2508.11542 (Aug. 2025). [arXiv:2508.11542](https://arxiv.org/abs/2508.11542), doi:10.48550/arXiv.2508.11542.

[13] M. Guo, S. A. McQuarrie, K. E. Willcox, Bayesian operator inference for data-driven reduced-order modeling, *Computer Methods in Applied Mechanics and Engineering* 402 (2022) 115336. doi:10.1016/j.cma.2022.115336.

[14] S. A. McQuarrie, A. Chaudhuri, K. E. Willcox, M. Guo, Bayesian learning with Gaussian processes for low-dimensional representations of time-dependent nonlinear systems, *Physica D: Nonlinear Phenomena* 475 (2025) 134572. doi:10.1016/j.physd.2025.134572.

[15] H. Sharma, Z. Wang, B. Kramer, Hamiltonian operator inference: Physics-preserving learning of reduced-order models for canonical Hamiltonian systems, *Physica D: Nonlinear Phenomena* 431 (2022) 133122. doi:10.1016/j.physd.2021.133122.

[16] H. Sharma, D. A. Najera-Flores, M. D. Todd, B. Kramer, Lagrangian operator inference enhanced with structure-preserving machine learning for nonintrusive model reduction of mechanical systems, *Computer Methods in Applied Mechanics and Engineering* 423 (2024) 116865.

[17] T. Koike, E. Qian, Energy-Preserving Reduced Operator Inference for Efficient Design and Control, in: AIAA SCITECH 2024 Forum, American Institute of Aeronautics and Astronautics, Orlando, FL, 2024, p. 1012. doi:10.2514/6.2024-1012.

[18] A. Gruber, I. Tezaur, Variationally Consistent Hamiltonian Model Reduction, *SIAM Journal on Applied Dynamical Systems* 24 (1) (2025) 376–414. doi:10.1137/24M1652490.

[19] P. Goyal, I. P. Duff, P. Benner, Guaranteed stable quadratic models and their applications in sindy and operator inference, *Physica D: Nonlinear Phenomena* (2025) 134893.

[20] Y. Shuai, C. W. Rowley, Symmetry-reduced model reduction of shift-equivariant systems via operator inference, arXiv preprint arXiv:2507.18780 (Jul. 2025). [arXiv:2507.18780](https://arxiv.org/abs/2507.18780), doi:10.48550/arXiv.2507.18780.

[21] B. G. Zastrow, A. Chaudhuri, K. E. Willcox, A. Ashley, M. C. Henson, Block-structured operator inference for coupled multiphysics model reduction, UT Austin (2025).

[22] A. Prakash, Y. J. Zhang, Nonintrusive projection-based reduced order modeling using stable learned differential operators, *Computer Methods in Applied Mechanics and Engineering* 442 (2025) 117946. doi:10.1016/j.cma.2025.117946.

[23] B. Peherstorfer, Sampling Low-Dimensional Markovian Dynamics for Preasymptotically Recovering Reduced Models from Data with Operator Inference, *SIAM Journal on Scientific Computing* 42 (5) (2020) A3489–A3515. doi:10.1137/19M1292448.

[24] W. I. T. Uy, Y. Wang, Y. Wen, B. Peherstorfer, Active Operator Inference for Learning Low-Dimensional Dynamical-System Models from Noisy Data, *SIAM Journal on Scientific Computing* 45 (4) (2023) A1462–A1490. doi:10.1137/21M1439729.

[25] E. Qian, B. Kramer, B. Peherstorfer, K. Willcox, Lift & Learn: Physics-informed machine learning for large-scale nonlinear dynamical systems, *Physica D: Nonlinear Phenomena* 406 (2020) 132401. doi:10.1016/j.physd.2020.132401.

[26] H. Rosenberger, B. Sanderse, G. Stabile, Exact operator inference with minimal data, arXiv preprint arXiv:2506.01244 (2025).

[27] E. Qian, I.-G. Farcaş, K. Willcox, Reduced Operator Inference for Nonlinear Partial Differential Equations, *SIAM Journal on Scientific Computing* 44 (4) (2022) A1934–A1959. doi:10.1137/21M1393972.

[28] Y. Filanova, I. Pontes Duff, P. Goyal, P. Benner, An operator inference oriented approach for linear mechanical systems, *Mechanical Systems and Signal Processing* 200 (2023) 110620. doi:10.1016/j.ymssp.2023.110620.

[29] A. Gruber, I. Tezaur, Canonical and noncanonical hamiltonian operator inference, *Computer Methods in Applied Mechanics and Engineering* 416 (2023) 116334.

[30] H. Sharma, B. Kramer, Preserving lagrangian structure in data-driven reduced-order modeling of large-scale dynamical systems, *Physica D: Nonlinear Phenomena* 462 (2024) 134128.

[31] Y. Geng, J. Singh, L. Ju, B. Kramer, Z. Wang, Gradient preserving Operator Inference: Data-driven reduced-order models for equations with gradient structure, *Computer Methods in Applied Mechanics and Engineering* 427 (2024) 117033. doi:10.1016/j.cma.2024.117033.

[32] H. Kim, B. Kramer, Physically consistent predictive reduced-order modeling by enhancing operator inference with state constraints, arXiv preprint arXiv:2502.03672 (2025).

[33] C. Gahr, I.-G. Farcaş, F. Jenko, Scientific machine learning based reduced-order models for plasma turbulence simulations, *Physics of Plasmas* 31 (11) (2024) 113904. doi:10.1063/5.0225584.

[34] B. G. Zastrow, A. Chaudhuri, K. E. Willcox, A. S. Ashley, M. C. Henson, Data-driven model reduction via operator inference for coupled aeroelastic flutter, in: AIAA Scitech 2023 Forum, 2023, p. 0330.

[35] O. Issan, B. Kramer, Predicting solar wind streams from the inner-heliosphere to Earth via shifted operator inference, *Journal of Computational Physics* 473 (2023) 111689. doi:10.1016/j.jcp.2022.111689.

[36] D. J. Lucia, P. S. Beran, W. A. Silva, Reduced-order modeling: new approaches for computational physics, *Progress in*

aerospace sciences 40 (1-2) (2004) 51–117.

[37] M. P. Mignolet, A. Przekop, S. A. Rizzi, S. M. Spottswood, A review of indirect/non-intrusive reduced order modeling of nonlinear geometric structures, *Journal of Sound and Vibration* 332 (10) (2013) 2437–2460.

[38] M. Guo, J. S. Hesthaven, Data-driven reduced order modeling for time-dependent problems, *Computer methods in applied mechanics and engineering* 345 (2019) 75–99.

[39] D. A. Randall, R. A. Wood, S. Bony, R. Colman, T. Fichefet, J. Fyfe, V. Kattsov, A. Pitman, J. Shukla, J. Srinivasan, et al., Climate models and their evaluation, in: *Climate change 2007: The physical science basis. Contribution of Working Group I to the Fourth Assessment Report of the IPCC (FAR)*, Cambridge University Press, 2007, pp. 589–662.

[40] C. Schär, O. Fuhrer, A. Arteaga, N. Ban, C. Charpiloz, S. Di Girolamo, L. Hentgen, T. Hoefer, X. Lapillonne, D. Leutwyler, et al., Kilometer-scale climate models: Prospects and challenges, *Bulletin of the American Meteorological Society* 101 (5) (2020) E567–E587.

[41] H. Hersbach, B. Bell, P. Berrisford, S. Hirahara, A. Horányi, J. Muñoz-Sabater, J. Nicolas, C. Peubey, R. Radu, D. Schepers, et al., The era5 global reanalysis, *Quarterly journal of the royal meteorological society* 146 (730) (2020) 1999–2049.

[42] K. Willcox, Model reduction for large-scale applications in computational fluid dynamics, in: *Real-Time PDE-Constrained Optimization*, SIAM, 2007, pp. 217–232.

[43] N. J. Georgiadis, D. P. Rizzetta, C. Fureby, Large-eddy simulation: current capabilities, recommended practices, and future research, *AIAA journal* 48 (8) (2010) 1772–1784.

[44] E. J. Nielsen, A. Walden, G. Nastac, L. Wang, W. Jones, M. Lohry, W. K. Anderson, B. Diskin, Y. Liu, C. L. Rumsey, et al., Large-scale computational fluid dynamics simulations of aerospace configurations on the frontier exascale system, in: *AIAA AVIATION FORUM AND ASCEND 2024*, 2024, p. 3866.

[45] W. Schmidt, Large eddy simulations in astrophysics, *Living Reviews in Computational Astrophysics* 1 (1) (2015) 2.

[46] B. Burkhardt, S. M. Appel, S. Bialy, J. Cho, A. J. Christensen, D. Collins, C. Federrath, D. B. Fielding, D. Finkbeiner, A. S. Hill, J. C. Ibáñez-Mejía, M. R. Krumholz, A. Lazarian, M. Li, P. Mocz, M.-M. Mac Low, J. Naiman, S. K. N. Portillo, B. Shane, Z. Slepian, Y. Yuan, The Catalogue for Astrophysical Turbulence Simulations (CATS), *The Astrophysical Journal* 905 (1) (2020) 14. doi:10.3847/1538-4357/abc484.

[47] R. E. Angulo, O. Hahn, Large-scale dark matter simulations, *Living Reviews in Computational Astrophysics* 8 (1) (2022) 1.

[48] R. Ohana, M. McCabe, L. Meyer, R. Morel, F. Agocs, M. Beneitez, M. Berger, B. Burkhardt, S. Dalziel, D. Fielding, et al., The well: a large-scale collection of diverse physics simulations for machine learning, *Advances in Neural Information Processing Systems* 37 (2024) 44989–45037.

[49] S. Muthukrishnan, Data streams: Algorithms and applications, *Foundations and Trends® in Theoretical Computer Science* 1 (2) (2005) 117–236.

[50] M. Torzoni, M. Tezzele, S. Mariani, A. Manzoni, K. E. Willcox, A digital twin framework for civil engineering structures, *Computer Methods in Applied Mechanics and Engineering* 418 (2024) 116584.

[51] S. Henneking, S. Venkat, V. Dobrev, J. Camier, T. Kolev, M. Fernando, A.-A. Gabriel, O. Ghattas, Real-time bayesian inference at extreme scale: A digital twin for tsunami early warning applied to the cascadia subduction zone, in: *Proceedings of the International Conference for High Performance Computing, Networking, Storage and Analysis*, 2025, pp. 60–71.

[52] K. Tomsovic, D. E. Bakken, V. Venkatasubramanian, A. Bose, Designing the next generation of real-time control, communication, and computations for large power systems, *Proceedings of the IEEE* 93 (5) (2005) 965–979.

[53] Z. Lan, Z. Zheng, Y. Li, Toward automated anomaly identification in large-scale systems, *IEEE Transactions on Parallel and Distributed Systems* 21 (2) (2009) 174–187.

[54] I.-G. Farcaş, R. P. Gundevia, R. Munipalli, K. E. Willcox, Distributed computing for physics-based data-driven reduced modeling at scale: Application to a rotating detonation rocket engine, *Computer Physics Communications* 313 (2025) 109619. doi:10.1016/j.cpc.2025.109619.

[55] R. Geelen, K. Willcox, Localized non-intrusive reduced-order modelling in the operator inference framework, *Philosophical Transactions of the Royal Society A: Mathematical, Physical and Engineering Sciences* 380 (2229) (2022) 20210206. doi:10.1098/rsta.2021.0206.

[56] I.-G. Farcas, R. P. Gundevia, R. Munipalli, K. E. Willcox, Domain Decomposition for Data-Driven Reduced Modeling of Large-Scale Systems, *AIAA Journal* (2024) 1–16doi:10.2514/1.J063715.

[57] I. Moore, C. Wentland, A. Gruber, I. Tezaur, Domain Decomposition-based coupling of Operator Inference reduced order models via the Schwarz alternating method, *arXiv preprint arXiv:2409.01433* (Oct. 2024). arXiv:2409.01433, doi:10.48550/arXiv.2409.01433.

[58] L. Gkimisis, N. Aretz, M. Tezzele, T. Richter, P. Benner, K. E. Willcox, Non-intrusive reduced-order modeling for dynamical systems with spatially localized features, *Computer Methods in Applied Mechanics and Engineering* 444 (2025) 118115. doi:10.1016/j.cma.2025.118115.

[59] P. Benner, E. S. Quintana-Ortí, G. Quintana-Ortí, Balanced truncation model reduction of large-scale dense systems on parallel computers, *Mathematical and Computer Modelling of Dynamical Systems* 6 (4) (2000) 383–405.

[60] H. Antil, M. Heinkenschloss, R. H. Hoppe, D. C. Sorensen, Domain decomposition and model reduction for the numerical solution of pde constrained optimization problems with localized optimization variables, *Computing and Visualization in Science* 13 (6) (2010) 249–264.

[61] D. J. Knezevic, J. W. Peterson, A high-performance parallel implementation of the certified reduced basis method, *Computer Methods in Applied Mechanics and Engineering* 200 (13–16) (2011) 1455–1466.

[62] S. Ares de Parga, J. Bravo, N. Sibuet, J. Hernandez, R. Rossi, S. Boschert, E. S. Quintana-Ortí, A. E. Tomás, C. C. Tatú, F. Vázquez-Novoa, et al., Parallel reduced-order modeling for digital twins using high-performance computing workflows, *Computers & Structures* 316 (2025) 107867. doi:<https://doi.org/10.1016/j.compstruc.2025.107867>.

[63] S. Perotto, A. Ern, A. Veneziani, Hierarchical local model reduction for elliptic problems: a domain decomposition approach, *Multiscale Modeling & Simulation* 8 (4) (2010) 1102–1127.

[64] C. Hoang, Y. Choi, K. Carlberg, Domain-decomposition least-squares petrov–galerkin (dd-lspg) nonlinear model reduction, *Computer methods in applied mechanics and engineering* 384 (2021) 113997.

[65] A. N. Diaz, Y. Choi, M. Heinkenschloss, A fast and accurate domain decomposition nonlinear manifold reduced order model, *Computer Methods in Applied Mechanics and Engineering* 425 (2024) 116943.

[66] C. Baker, K. Gallivan, P. Van Dooren, Low-rank incremental methods for computing dominant singular subspaces, *Linear Algebra and its Applications* 436 (8) (2012) 2866–2888. doi:[10.1016/j.laa.2011.07.018](https://doi.org/10.1016/j.laa.2011.07.018).

[67] J. A. Tropp, A. Yurtsever, M. Udell, V. Cevher, Streaming Low-Rank Matrix Approximation with an Application to Scientific Simulation, *SIAM Journal on Scientific Computing* 41 (4) (2019) A2430–A2463. doi:[10.1137/18M1201068](https://doi.org/10.1137/18M1201068).

[68] A. H. Sayed, *Adaptive Filters*, John Wiley & Sons, 2011.

[69] S. S. Haykin, *Adaptive Filter Theory*, fifth edition, international edition Edition, Always Learning, Pearson, Upper Saddle River Boston Columbus San Francisco New York, 2014.

[70] P. J. Schmid, Dynamic mode decomposition of numerical and experimental data, *Journal of Fluid Mechanics* 656 (2010) 5–28. doi:[10.1017/S0022112010001217](https://doi.org/10.1017/S0022112010001217).

[71] Aaron Towne, Oliver T. Schmidt, Tim Colonius, Spectral proper orthogonal decomposition and its relationship to dynamic mode decomposition and resolvent analysis, *Journal of Fluid Mechanics* 847 (2018) 821–867. doi:[10.1017/jfm.2018.283](https://doi.org/10.1017/jfm.2018.283).

[72] O. T. Schmidt, A. Towne, An efficient streaming algorithm for spectral proper orthogonal decomposition, *Computer Physics Communications* 237 (2019) 98–109. doi:[10.1016/j.cpc.2018.11.009](https://doi.org/10.1016/j.cpc.2018.11.009).

[73] P. Schwerdtner, P. Mohan, A. Pachalieva, J. Bessac, D. O’Malley, B. Peherstorfer, Online learning of quadratic manifolds from streaming data for nonlinear dimensionality reduction and nonlinear model reduction, *Proceedings of the Royal Society A: Mathematical, Physical and Engineering Sciences* 481 (2314) (2025) 20240670. doi:[10.1098/rspa.2024.0670](https://doi.org/10.1098/rspa.2024.0670).

[74] M. S. Hemati, M. O. Williams, C. W. Rowley, Dynamic mode decomposition for large and streaming datasets, *Physics of Fluids* 26 (11) (2014) 111701. doi:[10.1063/1.4901016](https://doi.org/10.1063/1.4901016).

[75] D. Matsumoto, T. Indinger, On-the-fly algorithm for Dynamic Mode Decomposition using Incremental Singular Value Decomposition and Total Least Squares, *arXiv preprint arXiv:1703.11004* (Mar. 2017). arXiv:1703.11004.

[76] J. Liew, T. Göçmen, W. H. Lio, G. C. Larsen, Streaming dynamic mode decomposition for short-term forecasting in wind farms, *Wind Energy* 25 (4) (2022) 719–734. doi:[10.1002/we.2694](https://doi.org/10.1002/we.2694).

[77] S. Anantharamu, K. Mahesh, A parallel and streaming Dynamic Mode Decomposition algorithm with finite precision error analysis for large data, *Journal of Computational Physics* 380 (2019) 355–377. doi:[10.1016/j.jcp.2018.12.012](https://doi.org/10.1016/j.jcp.2018.12.012).

[78] H. Zhang, C. W. Rowley, E. A. Deem, L. N. Cattafesta, Online Dynamic Mode Decomposition for Time-Varying Systems, *SIAM Journal on Applied Dynamical Systems* 18 (3) (2019) 1586–1609. doi:[10.1137/18M1192329](https://doi.org/10.1137/18M1192329).

[79] M. Alflatlawi, V. Srivastava, An incremental approach to online dynamic mode decomposition for time-varying systems with applications to EEG data modeling, *Journal of Computational Dynamics* 7 (2) (Tue Dec 01 00:00:00 UTC 2020) 209–241. doi:[10.3934/jcd.2020009](https://doi.org/10.3934/jcd.2020009).

[80] C. W. Rowley, I. Mezić, S. Bagheri, P. Schlatter, D. S. Henningson, Spectral analysis of nonlinear flows, *Journal of fluid mechanics* 641 (2009) 115–127.

[81] I. Mezić, Analysis of fluid flows via spectral properties of the koopman operator, *Annual review of fluid mechanics* 45 (1) (2013) 357–378.

[82] S. Sinha, S. P. Nandamoori, D. A. Barajas-Solano, Online real-time learning of dynamical systems from noisy streaming data, *Scientific Reports* 13 (1) (2023) 22564. doi:[10.1038/s41598-023-49045-w](https://doi.org/10.1038/s41598-023-49045-w).

[83] B. P. Russo, M. P. Laiu, R. Archibald, Streaming Compression of Scientific Data via Weak-SINDy, *SIAM Journal on Scientific Computing* 47 (1) (2025) C207–C234. doi:[10.1137/23M1599331](https://doi.org/10.1137/23M1599331).

[84] J. L. Lumley, The structure of inhomogeneous turbulent flows, *Atmospheric turbulence and radio wave propagation* (1967) 166–178.

[85] L. Sirovich, Turbulence and the dynamics of coherent structures. i. coherent structures, *Quarterly of applied mathematics* 45 (3) (1987) 561–571.

[86] G. Berkooz, P. Holmes, J. L. Lumley, The Proper Orthogonal Decomposition in the Analysis of Turbulent Flows, *Annual review of fluid mechanics* 25 (1) (1993) 539–575. doi:10.1146/annurev.fl.25.010193.002543.

[87] J. R. Bunch, C. P. Nielsen, Updating the singular value decomposition, *Numerische Mathematik* 31 (2) (1978) 111–129. doi:10.1007/BF01397471.

[88] M. Gu, S. Eisenstat, A Stable and Fast Algorithm for Updating the Singular Value Decomposition, Department of Computer Science, Yale University (1993).

[89] S. Chandrasekaran, B. S. Manjunath, Y. F. Wang, J. Winkeler, H. Zhang, An Eigenspace Update Algorithm for Image Analysis, *Graphical Models and Image Processing* 59 (5) (1997) 321–332. doi:10.1006/gmip.1997.0425.

[90] A. Levey, M. Lindenbaum, Sequential Karhunen-Loeve basis extraction and its application to images, *IEEE Transactions on Image Processing* 9 (8) (2000) 1371–1374. doi:10.1109/83.855432.

[91] M. Brand, Incremental Singular Value Decomposition of Uncertain Data with Missing Values, in: A. Heyden, G. Sparr, M. Nielsen, P. Johansen (Eds.), *Computer Vision — ECCV 2002*, Lecture Notes in Computer Science, Springer, Berlin, Heidelberg, 2002, pp. 707–720. doi:10.1007/3-540-47969-4_47.

[92] G. M. Oxberry, T. Kostova-Vassilevska, W. Arrighi, K. Chand, Limited-memory adaptive snapshot selection for proper orthogonal decomposition, *International Journal for Numerical Methods in Engineering* 109 (2) (2017) 198–217. doi:10.1002/nme.5283.

[93] H. Zha, H. D. Simon, On Updating Problems in Latent Semantic Indexing, *SIAM Journal on Scientific Computing* 21 (2) (1999) 782–791. doi:10.1137/S1064827597329266.

[94] N. Halko, P. G. Martinsson, J. A. Tropp, Finding Structure with Randomness: Probabilistic Algorithms for Constructing Approximate Matrix Decompositions, *SIAM Review* 53 (2) (2011) 217–288. doi:10.1137/090771806.

[95] J. A. Tropp, A. Yurtsever, M. Udell, V. Cevher, Supplementary Materials: Streaming Low-Rank Matrix Approximation with an Application to Scientific Simulation, *SIAM Journal on Scientific Computing* 41 (4) (2019) A2430–A2463. doi:10.1137/18M1201068.

[96] C. Eckart, G. Young, The approximation of one matrix by another of lower rank, *Psychometrika* 1 (3) (1936) 211–218.

[97] H. Fareed, J. R. Singler, Error analysis of an incremental proper orthogonal decomposition algorithm for PDE simulation data, *Journal of Computational and Applied Mathematics* 368 (2020) 112525. doi:10.1016/j.cam.2019.112525.

[98] J. Brewer, Kronecker products and matrix calculus in system theory, *IEEE Transactions on Circuits and Systems* 25 (9) (1978) 772–781. doi:10.1109/TCS.1978.1084534.

[99] C. G. Khatri, C. R. Rao, Solutions to Some Functional Equations and Their Applications to Characterization of Probability Distributions, *Sankhyā: The Indian Journal of Statistics, Series A* (1961–2002) 30 (2) (1968) 167–180. arXiv:25049527.

[100] C. R. Rao, Estimation of Heteroscedastic Variances in Linear Models, *Journal of the American Statistical Association* 65 (329) (1970) 161–172. arXiv:2283583, doi:10.2307/2283583.

[101] V. I. Slyusar, Analytical model of the digital antenna array on a basis of face-splitting matrixs product, in: *Proceedings of International Conference on Antenna Theory and Techniques*, 1997, pp. 108–109.

[102] L. Ljung, T. Söderström, *Theory and Practice of Recursive Identification*, Signal Processing, Optimization, and Control, MIT Press, Cambridge, MA, USA, 1987.

[103] K. Taira, S. L. Brunton, S. T. Dawson, C. W. Rowley, T. Colonius, B. J. McKeon, O. T. Schmidt, S. Gordeyev, V. Theofilis, L. S. Ukeiley, Modal analysis of fluid flows: An overview, *AIAA journal* 55 (12) (2017) 4013–4041.

[104] A. Stotsky, Recursive least squares estimation with rank two updates, *Automatika* 66 (4) (2025) 619–624.

[105] J. M. Burgers, A mathematical model illustrating the theory of turbulence, *Advances in applied mechanics* 1 (1948) 171–199.

[106] J. Degroote, J. Vierendeels, K. Willcox, Interpolation among reduced-order matrices to obtain parameterized models for design, optimization and probabilistic analysis, *International Journal for Numerical Methods in Fluids* 63 (2) (2010) 207–230. doi:10.1002/fld.2089.

[107] Å. Björck, G. H. Golub, Numerical Methods for Computing Angles Between Linear Subspaces, *Mathematics of Computation* 27 (123) (1973) 579–594. arXiv:2005662, doi:10.2307/2005662.

[108] Y. Kuramoto, Diffusion-induced chaos in reaction systems, *Progress of Theoretical Physics Supplement* 64 (1978) 346–367.

[109] G. I. Sivashinsky, Nonlinear analysis of hydrodynamic instability in laminar flames—i. derivation of basic equations, *Acta astronautica* 4 (11–12) (1977) 1207–1221.

[110] F. Lu, K. K. Lin, A. J. Chorin, Data-based stochastic model reduction for the kuramoto–sivashinsky equation, *Physica D: Nonlinear Phenomena* 340 (2017) 46–57.

[111] J. L. S. Almeida, A. C. Pires, K. F. V. Cid, A. C. Nogueira, Non-intrusive operator inference for chaotic systems, *IEEE Transactions on Artificial Intelligence* (2022) 1–14doi:10.1109/TAI.2022.3207449.

[112] J. C. Sprott, *Elegant chaos: algebraically simple chaotic flows*, World Scientific, 2010.

[113] J. Szezech Jr, S. Lopes, R. Viana, Onset of spatiotemporal chaos in a nonlinear system, *Physical Review E—Statistical, Nonlinear, and Soft Matter Physics* 75 (6) (2007) 067202.

[114] P. Cvitanović, R. L. Davidchack, E. Siminos, On the State Space Geometry of the Kuramoto–Sivashinsky Flow in a Periodic Domain, *SIAM Journal on Applied Dynamical Systems* 9 (1) (2010) 1–33. doi:10.1137/070705623.

[115] A. Wolf, J. B. Swift, H. L. Swinney, J. A. Vastano, Determining lyapunov exponents from a time series, *Physica D: nonlinear phenomena* 16 (3) (1985) 285–317.

[116] P. V. Kuptsov, U. Parlitz, Theory and computation of covariant lyapunov vectors, *Journal of nonlinear science* 22 (5) (2012) 727–762.

[117] M. Sandri, Numerical calculation of lyapunov exponents, *Mathematica Journal* 6 (3) (1996) 78–84.

[118] J. L. Kaplan, J. A. Yorke, Chaotic behavior of multidimensional difference equations, in: *Functional Differential Equations and Approximation of Fixed Points: Proceedings, Bonn, July 1978*, Springer, 2006, pp. 204–227.

[119] K. E. Chlouverakis, J. Sprott, A comparison of correlation and Lyapunov dimensions, *Physica D: Nonlinear Phenomena* 200 (1-2) (2005) 156–164. doi:10.1016/j.physd.2004.10.006.

[120] R. A. Edson, J. E. Bunder, T. W. Mattner, A. J. Roberts, Lyapunov Exponents of the Kuramoto-Sivashinsky PDE, *The ANZIAM Journal* 61 (3) (2019) 270–285. doi:10.1017/S1446181119000105.

[121] M. B. Kuhn, M. T. Henry de Frahan, P. Mohan, G. Deskos, M. Churchfield, L. Cheung, A. Sharma, A. Almgren, S. Ananthan, M. J. Brazell, et al., Amr-wind: A performance-portable, high-fidelity flow solver for wind farm simulations, *Wind Energy* 28 (5) (2025) e70010.

[122] A. Sharma, M. J. Brazell, G. Vijayakumar, S. Ananthan, L. Cheung, N. deVelder, M. T. Henry de Frahan, N. Matula, P. Mullowney, J. Rood, P. Sakievich, A. Almgren, P. S. Crozier, M. Sprague, Exawind: Open-source cfd for hybrid-rans/les geometry-resolved wind turbine simulations in atmospheric flows, *Wind Energy* 27 (3) (2024) 225–257. arXiv:<https://onlinelibrary.wiley.com/doi/pdf/10.1002/we.2886>, doi:10.1002/we.2886.

[123] J. Bredberg, On the wall boundary condition for turbulence models, Chalmers University of Technology, Department of Thermo and Fluid Dynamics, Internal Report 00/4. Goteborg (2000) 8–16.

[124] M. Kadivar, D. Tormey, G. McGranaghan, A review on turbulent flow over rough surfaces: Fundamentals and theories, *International Journal of Thermofluids* 10 (2021) 100077.

[125] R. D. Moser, J. Kim, N. N. Mansour, et al., Direct numerical simulation of turbulent channel flow up to $re=590$, *Phys. fluids* 11 (4) (1999) 943–945.

[126] B. Pinier, E. Mémin, S. Laizet, R. Lewandowski, Stochastic flow approach to model the mean velocity profile of wall-bounded flows, *Physical Review E* 99 (6) (2019) 063101.

[127] I. Marusic, J. P. Monty, M. Hultmark, A. J. Smits, On the logarithmic region in wall turbulence, *Journal of Fluid Mechanics* 716 (2013) R3.

[128] P.-Å. Wedin, Perturbation theory for pseudo-inverses, *BIT Numerical Mathematics* 13 (2) (1973) 217–232.

[129] Y. Fang, K. A. Loparo, X. Feng, Inequalities for the trace of matrix product, *IEEE Transactions on Automatic Control* 39 (12) (1994) 2489–2490.

[130] G. H. Golub, C. F. Van Loan, *Matrix Computations*, fourth edition Edition, Johns Hopkins Studies in the Mathematical Sciences, The Johns Hopkins University Press, Baltimore, 2013.

[131] P. Lancaster, H. K. Farahat, Norms on direct sums and tensor products, *mathematics of computation* 26 (118) (1972) 401–414.

[132] R. A. Horn, C. R. Johnson, *Topics in matrix analysis*, Cambridge university press, 1994.